Comparisons of two receptor-MAPK pathways in a single cell-type reveal mechanisms of signalling specificity

Yan Ma, Isabelle Flückiger, Jade Nicolet, Jia Pang, Joe Dickinson, Damien de Bellis, Aurélia Emonet, Satoshi Fujita, Niko Geldner

To cite this version:

Yan Ma, Isabelle Flückiger, Jade Nicolet, Jia Pang, Joe Dickinson, et al.. Comparisons of two receptor-MAPK pathways in a single cell-type reveal mechanisms of signalling specificity. Nature Plants, 2024, 10 (9), pp.1343-1362. 10.1038/s41477-024-01768-y . hal-04705751

HAL Id: hal-04705751
https://cnrs.hal.science/hal-04705751v1

Submitted on 23 Sep 2024

nature plants

Article

https://doi.org/10.1038/s41477-024-01768-y

Comparisons of two receptor-MAPK pathways in a single cell-type reveal mechanisms of signalling specificity

Received: 1 September 2023

Accepted: 19 July 2024

Yan Ma[1,2,6], Isabelle Flückiger[1], Jade Nicolet[1], Jia Pang[1], Joe B. Dickinson[1,3], Damien De Bellis[1], Aurélia Emonet[1,4], Satoshi Fujita[1,5] & Niko Geldner[1,6]

Cells harbour numerous receptor pathways to respond to diverse stimuli, yet often share common downstream signalling components. Mitogen-activated protein kinase (MPK) cascades are an example of such common hubs in eukaryotes. How such common hubs faithfully transduce distinct signals within the same cell-type is insufficiently understood, yet of fundamental importance for signal integration and processing in plants. We engineered a unique genetic background allowing direct comparisons of a developmental and an immunity pathway in one cell-type, the *Arabidopsis* root endodermis. We demonstrate that the two pathways maintain distinct functional and transcriptional outputs despite common MPK activity patterns. Nevertheless, activation of different MPK kinases and MPK classes led to distinct functional readouts, matching observed pathway-specific readouts. On the basis of our comprehensive analysis of core MPK signalling elements, we propose that combinatorial activation within the MPK cascade determines the differential regulation of an endodermal master transcription factor, MYB36, that drives pathway-specific gene activation.

Multicellular organisms rely on individual cells to detect different stimuli and translate them into various biological responses. Correspondence must be maintained between an extracellular input and its specific cellular response output. Decades of research established chains of molecular events from ligand perception by cell surface receptors to transcriptional outputs in the nucleus. Yet a key question remains: how is pathway-specific information maintained all the way to the nucleus, when multiple receptor pathways are stimulated and converge on a limited number of common signalling intermediates? The mitogen-activated protein kinase (MPK) cascade is a key intermediate module, responding to numerous stimuli in plants, animals and fungi, leading to a diverse array of outputs[1–4]. Understanding the mechanisms underlying specificity in such an hourglass architecture presents a substantial challenge.

In plants, this 'hourglass problem' is amplified due to their cell types being more broadly competent, compared with highly specialized mammalian cells. *Arabidopsis*, for instance, displays over 200 leucine-rich-repeat receptor-like kinases (LRR-RLKs)[5,6], dwarfing the 11 Toll-like receptors found in humans[7], both representing a subset of their total receptor complement. At the same time, *Arabidopsis* has much less cell types than any mammal[8,9], enhancing the potential complexity of receptor pathways on a per-cell basis. In plants, a prevailing notion is that common pathway components mediate specific outputs by activating different sets of transcription factors, expressed in different cell types. Yet, this would imply that a single cell-type would accommodate only one receptor/ligand pathway, which is implausible for plant cells. Therefore, it is crucial to understand how different receptors in a single

---

[1]Department of Plant Molecular Biology, Biophore, UNIL-Sorge, University of Lausanne, Lausanne, Switzerland. [2]Present address: Gregor Mendel Institute of Molecular Plant Biology (GMI), Austrian Academy of Sciences, Vienna BioCenter, Vienna, Austria. [3]Present address: Department of Fundamental Microbiology, Biophore, UNIL-Sorge, University of Lausanne, Lausanne, Switzerland. [4]Present address: Max Planck Institute for Plant Breeding Research, Cologne, North Rhine-Westphalia, Germany. [5]Present address: Plant Science Research Laboratory (LRSV), UMR5546 CNRS/Université Toulouse 3, Auzeville Tolosane, France. [6]These authors jointly supervised this work: Yan Ma, Niko Geldner. e-mail: Yan.ma@gmi.oeaw.ac.at; Niko.Geldner@unil.ch

plant cell maintain signalling specificity. However, such studies are scarce due to the challenges of isolating and analysing signalling events at single-cell resolution, as well as the lack of precise cellular readouts.

To address these challenges, we leveraged the ordered, linear differentiation of transparent *Arabidopsis* roots, allowing direct observation of single cells within an intact organism. Within this context, we established the *Arabidopsis* root endodermis as a cellular model to compare two well-studied LRR-RLK receptor pathways at single-cell level (Fig. 1a). One pathway uses the FLAGELLIN SENSING2 (FLS2) immune receptor, recognizing the microbial pattern flg22 (refs. 10,11). The other pathway uses the SCHENGEN3 (SGN3, also called GASSHO1 (GSO1)) receptor and its endogenous Casparian Strip Integrity Factor 1/2 (CIF1/2) ligands[12,13]. The endodermis is a specialized cell layer found in all vascular plants, forming a ring-like Casparian strip (CS), a highly localized membrane–cell wall nexus (Fig. 1d) analogous to tight junctions in animal intestinal epithelia[14]. This CS is composed of a lignified cell wall, creating an extracellular diffusion barrier in roots[15,16]. SGN3 enables the plant to detect developmental or stress-induced discontinuities in its CS, manifested as CIF peptide leakage from inner cell layers[12,17]. During endodermal differentiation, the SGN3 pathway drives CS maturation, characterized by fusion of its membrane domains. In situations of chronic or strong stimulation, the SGN3 pathway additionally induces ectopic lignification of cell corners and excess suberization (Fig. 1a)[18–20]. These precise and distinctive subcellular features of the SGN3 pathway were used as unambiguous and quantifiable signalling readouts.

The SGN3 and FLS2 pathways are regarded to have markedly different functional outputs (a precise developmental programme versus a broad bacterial immune response), yet they display striking similarities in the downstream signalling components. Both receptors use the same small family of co-receptors to bind their respective ligands, flg22 and CIF2 (refs. 21–23). Both require members of the same small family of SERK co-receptors[23,24] and subsequently activate members of the receptor-like cytoplasmic kinase VII family[20,25], which triggers a series of common intracellular signalling events, including reactive oxygen species (ROS) production and activation of MPKs[20,26–29]. How are different outputs achieved when pathways share such extensive similarities? Narrowing the broad expression of FLS2 into the endodermal SGN3 domain sharpens the question of signalling specificity in plants, because it finally allows us to address what happens when two pathways are stimulated in a single cell-type.

Using our tailored genetic background, we provide clear evidence for the maintenance of signalling specificity in a single cell despite strong pathway activation. We identify the transcription factor MYB36, a master regulator of endodermal differentiation[19,30], as a key hub driving pathway-specific outputs in the nucleus. Through extensive, cell-type-specific loss and gain-of-function studies of MPKs and MPK kinases (MKKs), we unveil their distinct capacities for transducing both common and specific branches of the two signalling pathways. We demonstrate that so-called 'common intermediates', such as MPK cascades, can produce a wide range of outputs through combinatorial activation of common and specific components.

Endodermis-specific FLS2 cannot replace endogenous SGN3 for CS domain fusion

To allow stimulation and direct comparison of two distinct pathways in the differentiating root endodermis (Fig. 1a), we expressed FLS2 under the endodermis-specific SGN3 promoter (pSGN3::FLS2-GFP) in an *fls2* mutant background (Fig. 1b). We then knocked out *CIF1* and *CIF2* genes using CRISPR-Cas9, ensuring that SGN3 signalling only occurs upon external peptide stimulation. We termed the resulting plant line (*pSGN3::FLS2-GFP fls2 cif1 cif2)* as '*2-in-Endo*'. CIF2 peptide treatments on the *cif1 cif2* mutant can efficiently restore the SGN3 pathway function and re-establish a continuous Casparian strip[20,23]; flg22 peptide treatments rapidly activate immune signalling in the endodermis from both native[31] and endodermis-expressed FLS2 in the root[31,32]. Using this line, we investigated whether FLS2 could functionally replace SGN3.

SGN3 pathway stimulation causes growth and fusion of the Casparian strip domains (CSD) from aligned islands (called 'string-of-pearls' stage) into a continuous belt (Fig. 1d)[12,13,33]. Casparian strip domain protein 1 (CASP1) marks this domain and predicts lignin deposition at the CS[26,34]. We therefore introduced pCASP1::CASP1-GFP (CASP1-GFP) into *2-in-Endo*. We confirmed that CIF2 treatment triggers full connection of CASP1 domains and corresponding CS lignin, leaving no gaps at a stage where the CS is fully mature in wild-type roots (Fig. 1c,d and Supplementary Video 1). In contrast, treatments with flg22 cannot improve CS domain fusion, showing comparable percentage of gap areas to controls (Fig. 1e). This was confirmed by visualizing CASP1-GFP from initiation to maturation (Extended Data Fig. 1a) and by quantifying discontinuity in overviews (Extended Data Fig. 1b,c).

Importantly, this distinct outcome is not due to a lack of FLS2 functionality, as flg22 treatment induces similar ROS production and ectopic lignification as CIF2 treatment (Fig. 1c and Extended Data Fig. 1f). These additional SGN3 pathway outcomes are also observed upon strong CIF2 stimulation[12,20]. A third outcome of strong CIF2 stimulation is precocious (nearer to the root tip) suberin deposition, also mimicked by flg22 treatment in *2-in-Endo* (Fig. 1a and Extended Data Fig. 1d). Therefore, endodermis-specific FLS2 signalling is able to replicate some outcomes of SGN3, but is unable to mediate the crucial aspect of CASP and CS domain growth and fusion. Even with higher FLS2 receptor levels in an *sgn3* background (*pCASP1::FLS2-GFP fls2 sgn3*, Fig. 1b), FLS2 stimulation cannot induce CASP domain fusion (Extended Data Fig. 1g,h).

This suggests that CS domain fusion is insensitive to FLS2 signalling, clearly indicating the presence of a main SGN3 signalling branch that FLS2 stimulation cannot induce.

Fig. 1 | Endodermis-specific FLS2 induces ectopic lignin but cannot replace endogenous SGN3 for Casparian strip domain fusion. a, A single cell-type signalling system in the root endodermis, comparing the SGN3/CIF2 developmental pathway and FLS2/flg22 immunity pathway. **b**, Endodermis-specific expression and localization of SGN3 (*pSGN3::SGN3-mVenus* in wild type) and FLS2-GFP under *pSGN3* or *pCASP1* in *fls2* or *fls2 sgn3* backgrounds. Representative overviews (maximum projection) and zoomed surface views (see **d**) of mature CS root cells are shown. This experiment was repeated twice with similar results. Colour bar shows gradient intensity of GFP and mVenus (mV). **c**, CS and CASP1 domain fusion in *2-in-Endo CASP1-GFP* after 1 d treatment with H_2O, 100 nM CIF2 or flg22. Left: Untreated *2-in-Endo* root scan outlined by calcofluor white staining of cellulosic cell walls (black). Endodermal cell surface views (see **d**) at mature CS stage (16th–17th endodermal cell after onset of elongation abbreviated 16th–17th cell) show CASP1-GFP (green), lignin stained with basic fuchsin (magenta) and overlaps of the two channels (Merged). Note that FLS2-GFP fluorescence is too weak to be detected with the same settings used to detect CASP1-GFP. Arrowheads highlight ectopic lignin. 'Outer', cortex-facing; 'inner', stele-facing endodermal surface. Scale bars, 5 µm. **d**, Schematics of CS development and three-dimensional architecture. Top left: Wild-type root shows CS maturation from disconnected domains to fused rings, functioning as a root apoplastic barrier. Early maturation occurs around the 11th–12th cell (mostly fused), while the 16th–17th cell reaches full maturity (fully fused). Right: SGN3 pathway mutants cannot fuse the CS domains and lack a functional barrier. Bottom: *2-in-Endo* fuses the CS domains in response to CIF2, but not to flg22, yet both trigger ectopic lignin (black arrowheads) at the cortex side. Illustrations adapted from ref. 20 under a Creative Commons license CC BY 4.0. **e**, Quantifications for **c** showing the percentage CASP1-GFP gaps in *2-in-Endo* in response to 1 d treatment with H_2O, 100 nM and 1 µM CIF2 or flg22 ($n \geq 8$ individual roots). **f**, PI penetration assay quantifies CS barrier function in *2-in-Endo* after 1 d treatments compared to controls ($n \geq 10$ individual roots). Roots with no barrier show PI penetration near the root–hypocotyl junction, shown in the 'near hypocotyl' category and are excluded from numerical statistical tests. For **e** and **f**, groups with the same letter are not significantly different ($P < 0.05$, one-way ANOVA and unbalanced Tukey's test for unequal replication).

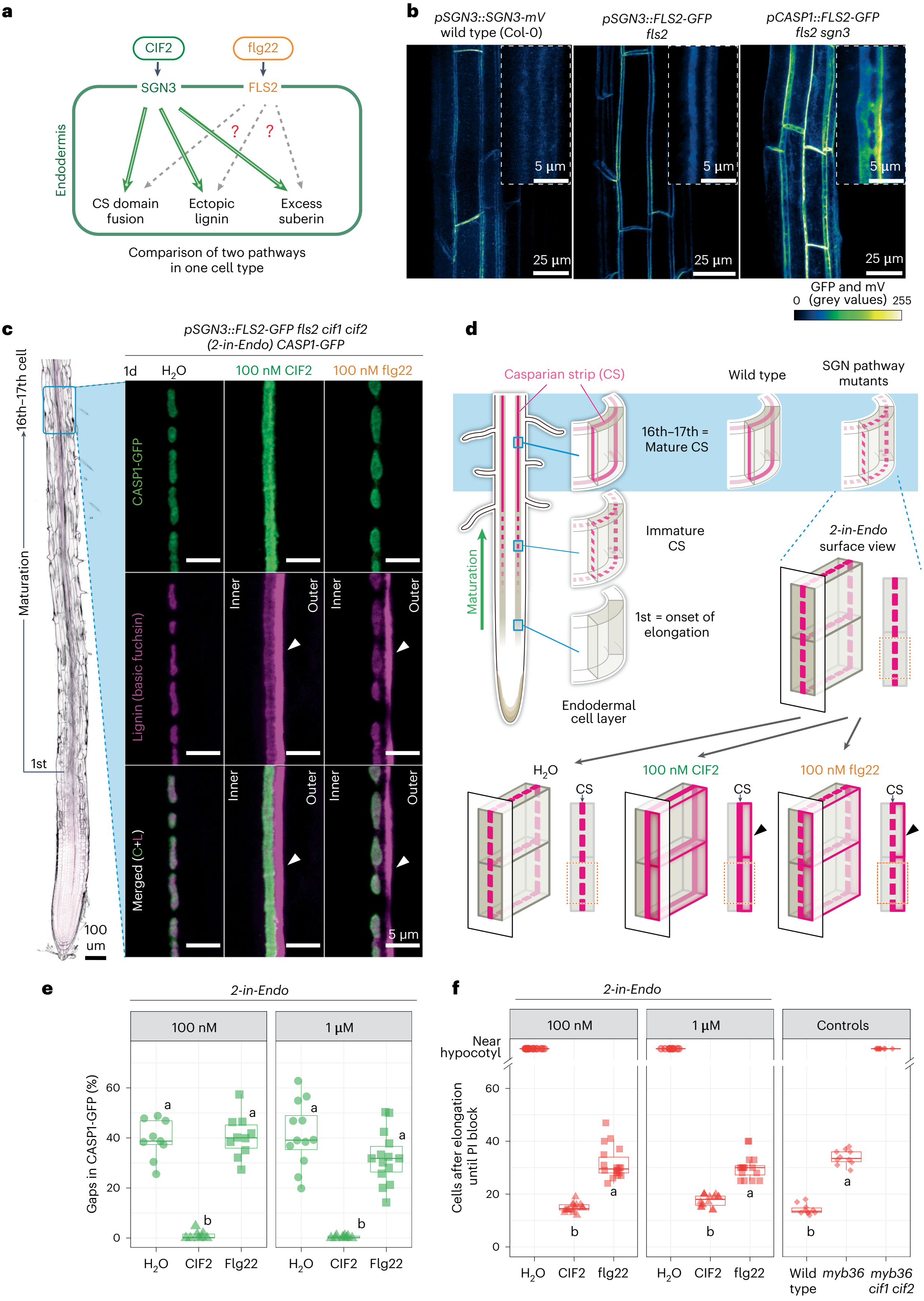
a
CIF2
flg22
SGN3
FLS2
Endodermis
?
?
CS domain fusion
Ectopic lignin
Excess suberin
Comparison of two pathways in one cell type
b
pSGN3::SGN3-mV wild type (Col-0)
pSGN3::FLS2-GFP fls2
pCASP1::FLS2-GFP fls2 sgn3
5 µm
25 µm
GFP and mV (grey values)
0
255
c
pSGN3::FLS2-GFP fls2 cif1 cif2 (2-in-Endo) CASP1-GFP
16th–17th cell
Maturation
1st
100 um
1d
H_2O
100 nM CIF2
100 nM flg22
CASP1-GFP
Lignin (basic fuchsin)
Merged (C+L)
Inner
Outer
5 µm
d
Casparian strip (CS)
Wild type
SGN pathway mutants
16th–17th = Mature CS
Immature CS
1st = onset of elongation
Endodermal cell layer
Maturation
2-in-Endo surface view
H_2O
100 nM CIF2
100 nM flg22
CS
e
2-in-Endo
100 nM
1 µM
Gaps in CASP1-GFP (%)
0
20
40
60
a
b
a
H_2O
CIF2
Flg22
f
2-in-Endo
100 nM
1 µM
Controls
Near hypocotyl
Cells after elongation until PI block
0
20
40
60
b
a
H_2O
CIF2
flg22
Wild type
myb36
myb36 cif1 cif2

Blocking of the propidium iodide (PI) fluorescent tracer provides a sensitive assay to measure CS functionality—it quantifies onset of an operational extracellular diffusion barrier by scoring PI exclusion from the inner vascular tissues (Extended Data Fig. 1e)[15,16]. In wild-type roots, blocking of PI uptake coincides with the formation of a continuous CS, assured by a functional SGN3 pathway (Fig. 1f). A delayed PI exclusion can still occur in the absence of a CS through SGN pathway-induced compensatory lignification at cell corners. This is observed in *myb36*, a CS-lacking mutant, but not in *myb36 cif1 cif2* (Fig. 1f). Note that the PI block in *myb36* is achieved purely by compensatory lignin, as the mutant lacks any CS lignin (Fig. 3b)[19]. This blockage is typically delayed by ~20 cells compared with wild-type plants with a CS (Fig. 1f).

We found that absence of a diffusion barrier in *2-in-Endo* (H_2O treatment) is fully rescued by CIF2 treatment, restoring a wild-type diffusion barrier (Fig. 1f and Extended Data Fig. 1e). By contrast, flg22 treatments activate delayed barrier formation in *2-in-Endo*, similar to *myb36*, through ectopic lignin formation (Fig. 1f). In the overexpressing *pCASP1::FLS2* line, the diffusion barrier is established earlier by flg22 (Extended Data Fig. 1i), probably due to stronger ectopic lignification (Extended Data Fig. 1g). Nevertheless, in both cases, barriers are still significantly delayed compared with CIF2-stimulated *2-in-Endo* or wild-type lines.

Thus, despite being able to induce lignification and suberization in the endodermis, FLS2 signalling cannot functionally replace SGN3 for the growth and fusion of CASP1 and CS domains, indicating that signalling specificity between two similar receptor pathways is maintained within the same cell-type.

Endodermis-expressed FLS2 and SGN3 activate both common and pathway-specific transcriptional responses

To compare transcriptional outputs of FLS2 and SGN3 pathways solely within the endodermis, we conducted comparative RNA-seq analysis of *pCASP1::FLS2 fls2* and wild-type seedling roots respectively treated with flg22 and CIF2 at three timepoints (30, 120, 480 min) (Extended Data Fig. 2a, CIF2 responses data from ref. 20). The receptor mutant controls *sgn3* and *fls2*, and displayed minimal gene responses to respective peptides (Fig. 2a). We found a substantial overlap between the SGN3 and the FLS2 pathway, with 469 out of 1,262 differentially expressed (DE) genes in common (Fig. 2a). The most enriched Gene Ontology (GO) categories of both pathways show a high degree of overlap, reflecting general biotic and abiotic stress responses (Fig. 2b). The shared functional outcomes that we observed are reflected in the transcriptional profiles: genes involved in lignin and suberin biosynthesis show matching induction patterns after CIF2 or flg22 treatment in the respective backgrounds (Fig. 2c,d). This commonality cannot be simply attributed to shared cell identity (the endodermis), as a cross analysis of highly flg22-responsive genes in whole wild-type seedlings[35] reveals mirrored induction patterns in the endodermis (Extended Data Fig. 2b).

Despite this overlap, we found 158 and 635 DE genes and GO terms specifically associated with SGN3 and FLS2 pathways, respectively (Fig. 2a and Extended Data Fig. 2d). The greater number of DE genes in the FLS2 pathway could arise from the stronger endodermal CASP1 promoter driving FLS2, compared with the native SGN3 promoter. To validate pathway-specific response genes (Extended Data Fig. 2c), we generated transcriptional fluorescent reporters in *2-in-Endo* and found that the majority of reporter lines match the RNA-seq predictions (Extended Data Fig. 2c and Supplementary Table 1). For example, *MILDEW RESISTANCE LOCUS O 3* (*MLO3*) shows a much stronger transcriptional response to CIF2 than to flg22 (Fig. 2f). Other SGN preferential reporter genes include *PRK1*, *LAC3* and *MCA2* (Supplementary Table 1 and Video 2). In contrast, the cytochrome P450 family gene *CYP715A1* is an FLS2-specific reporter that responds strongly to flg22 but is non-responsive to CIF2 (Fig. 2f), with other examples including *WRKY30*, *LAC1* and *PER52* (Supplementary Table 1 and Video 3). Some reporters respond equally well to either flg22 or CIF2 in *2-in-Endo*, with many showing non-cell-autonomous responses in surrounding root cell-types (for example, *WRKY41*, *PER71* and *ERF105*) (Supplementary Table 1).

Intriguingly, our dataset revealed that the top 10% most responsive genes (by fold change) in early timepoints are common to both pathways, whereas genes responding more weakly (but significantly) exhibited more pathway specificity (Extended Data Fig. 2e). We speculate that 'fast and strong' responses are often regulated by the common signalling modules of the two pathways.

The transcription factor MYB36 controls SGN3-specific transcriptional responses

Our transcriptional analyses suggested that the transcription factor MYB36, reported to be a key regulator of endodermis differentiation[19,30], also acts as a hub to regulate SGN3-specific responses. We found that genes regulated by MYB36 (downregulated in *myb36* compared with wild type[30]) tend to respond specifically to CIF2 (Fig. 2e). While the scale of induction by CIF2 is relatively weak ($\log_2$ FC < 2), many of these genes are specifically expressed in the endodermis and are known to contribute to CS integrity. For example, expression of *CASP* genes (*CASP1/2/3/4*) is crucial for establishing a functional CSD[34,36], while peroxidases such as PER9 and PER64 mediate CS lignification[37], and the dirigent protein ESB1 is essential for both CSD formation and lignification[38]. These genes might therefore carry out SGN3-specific functions and their non-responsiveness to flg22 can straightforwardly explain the inability of flg22 to promote CS domain fusion.

CIF2-induced CASP domain fusion requires de novo protein synthesis[20]. We hypothesize that MYB36-mediated transcriptional responses upon SGN3 stimulation enable CASP domain fusion, while the FLS2 pathway is incapable of activating MYB36. Consequently, the SGN3 pathway would function independently of MYB36 for ectopic lignification but require MYB36 for CASP and CS domain fusion. MYB36 remains partially functional in *sgn3* and *cif1 cif2*, but only mediates formation of aligned CASP domain islands. The role of SGN3 would therefore be to drive domain fusion by boosting the activity of MYB36.

Predicted MPK phospho-sites in MYB36 are important for CS domain fusion

MYB36 was shown to be phosphorylated by specific MPKs (MPKs 2, 3 and 16) in an in vitro protein microarray[39]. Three MPK phosphorylation motifs (serine proline) are predicted in MYB36 (Extended Data Fig. 3a). To test the potential necessity and sufficiency of MYB36 phosphorylation at these sites for CS domain fusion, we mutated all three serines

Fig. 2 | Endodermis-expressed FLS2 and SGN3 trigger common and pathway-specific transcriptional responses. a, Number of genes significantly regulated by CIF2 or flg22. Cut-off: $|\log_2$ fold change (FC)$| > 1$ and $P < 0.05$ for at least one timepoint. Genes that are significantly regulated by one pathway but not the other are considered specific. 'WT.CIF2', '*sgn3*.CIF2': wild-type/*sgn3* + 1 µM CIF2; 'FLS2.flg22', '*fls2*.flg22': pCASP1::FLS2-GFP *fls2*/*fls2* + 1 µM flg22. See Supplementary Fig. 2a for setup. **b**, GO-enrichment analysis of FLS2 and SGN3 pathways in endodermis. Colour: GO-enrichment significance. **c**,**d**, Heat maps of lignin (**c**) and suberin (**d**) biosynthesis-related gene expression fold changes post-peptide versus H_2O treatment at indicated timepoints. **e**, Heat maps of fold changes for MYB36-regulated genes, significantly downregulated in *myb36* compared with wild-type ($P < 0.001$). For **c**–**e**, asterisks indicate significant regulation ($P < 0.05$). Colour bar: degree of fold change. **f**, Time-lapse images of *pMLO3::NLS-3xmVenus* (top) and *pCYP715A1::NLS-3xmScarlet* (bottom) transcriptional responses in *2-in-Endo* to 1 µM CIF2 or flg22. Sum slice projections of roots at 3rd–7th cell (top) and 21st–25th cell (bottom) shown. Colour bar shows gradient intensity of mV or mScarlet (mS). Scale bars, 25 µm. Right: Quantifications show total grey intensity of nuclei signal at each hour (mean ± s.e., $n = 6$ individual roots).

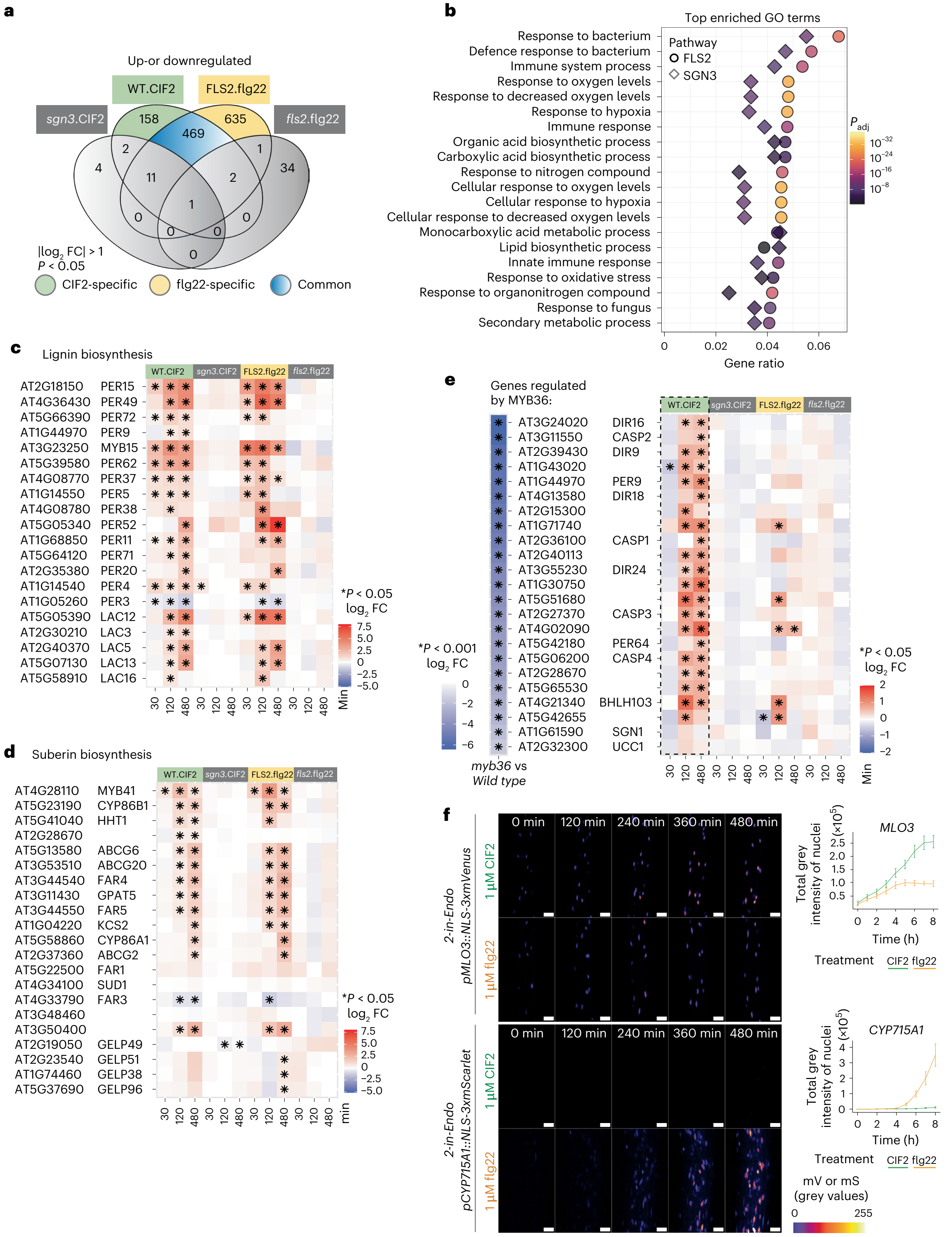
a
Up-or downregulated
WT.CIF2
FLS2.flg22
sgn3.CIF2
fls2.flg22
158
469
635
4
2
11
2
1
34
1
0
0
0
0
0
|log$_2$ FC| > 1
P < 0.05
CIF2-specific
flg22-specific
Common
b
Top enriched GO terms
Pathway
FLS2
SGN3
Response to bacterium
Defence response to bacterium
Immune system process
Response to oxygen levels
Response to decreased oxygen levels
Response to hypoxia
Immune response
Organic acid biosynthetic process
Carboxylic acid biosynthetic process
Response to nitrogen compound
Cellular response to oxygen levels
Cellular response to hypoxia
Cellular response to decreased oxygen levels
Monocarboxylic acid metabolic process
Lipid biosynthetic process
Innate immune response
Response to oxidative stress
Response to organonitrogen compound
Response to fungus
Secondary metabolic process
P_{adj}
10^{-32}
10^{-24}
10^{-16}
10^{-8}
0
0.02
0.04
0.06
Gene ratio
c
Lignin biosynthesis
WT.CIF2 sgn3.CIF2 FLS2.flg22 fls2.flg22
AT2G18150 PER15
AT4G36430 PER49
AT5G66390 PER72
AT1G44970 PER9
AT3G23250 MYB15
AT5G39580 PER62
AT4G08770 PER37
AT1G14550 PER5
AT4G08780 PER38
AT5G05340 PER52
AT1G68850 PER11
AT5G64120 PER71
AT2G35380 PER20
AT1G14540 PER4
AT1G05260 PER3
AT5G05390 LAC12
AT2G30210 LAC3
AT2G40370 LAC5
AT5G07130 LAC13
AT5G58910 LAC16
*P < 0.05
log$_2$ FC
7.5
5.0
2.5
0
−2.5
−5.0
30 120 480 30 120 480 30 120 480 30 120 480 Min
d
Suberin biosynthesis
WT.CIF2 sgn3.CIF2 FLS2.flg22 fls2.flg22
AT4G28110 MYB41
AT5G23190 CYP86B1
AT5G41040 HHT1
AT2G28670
AT5G13580 ABCG6
AT3G53510 ABCG20
AT3G44540 FAR4
AT3G11430 GPAT5
AT3G44550 FAR5
AT1G04220 KCS2
AT5G58860 CYP86A1
AT2G37360 ABCG2
AT5G22500 FAR1
AT4G34100 SUD1
AT4G33790 FAR3
AT3G48460
AT3G50400
AT2G19050 GELP49
AT2G23540 GELP51
AT1G74460 GELP38
AT5G37690 GELP96
*P < 0.05
log$_2$ FC
7.5
5.0
2.5
0
−2.5
−5.0
30 120 480 30 120 480 30 120 480 30 120 480 min
e
Genes regulated by MYB36:
WT.CIF2 sgn3.CIF2 FLS2.flg22 fls2.flg22
AT3G24020 DIR16
AT3G11550 CASP2
AT2G39430 DIR9
AT1G43020
AT1G44970 PER9
AT4G13580 DIR18
AT2G15300
AT1G71740
AT2G36100 CASP1
AT2G40113
AT3G55230 DIR24
AT1G30750
AT5G51680
AT2G27370 CASP3
AT4G02090
AT5G42180 PER64
AT5G06200 CASP4
AT2G28670
AT5G65530
AT4G21340 BHLH103
AT5G42655
AT1G61590 SGN1
AT2G32300 UCC1
*P < 0.001
log$_2$ FC
0
−2
−4
−6
myb36 vs Wild type
*P < 0.05
log$_2$ FC
2
1
0
−1
−2
30 120 480 30 120 480 30 120 480 30 120 480 Min
f
0 min 120 min 240 min 360 min 480 min
2-in-Endo pMLO3::NLS-3xmVenus
1 µM CIF2
1 µM flg22
2-in-Endo pCYP715A1::NLS-3xmScarlet
MLO3
Total grey intensity of nuclei (×10^5)
2.5
2.0
1.5
1.0
0.5
0 2 4 6 8
Time (h)
Treatment CIF2 flg22
CYP715A1
4
3
2
1
0
mV or mS (grey values)
0
255

to generate a phospho-null variant, MYB36$^{\text{AAA}}$ and a phosphomimic variant, MYB36$^{\text{DDD}}$.

The untagged MYB36$^{\text{AAA}}$, introduced in *myb36* mutant, can restore CASP1 expression and accumulation in the endodermis, but often failed to complement CASP1 domain fusion (Fig. 3a and Supplementary Table 2). This suggests that MYB36$^{\text{AAA}}$, while active, is less functional than either the wild-type MYB36$^{\text{WT}}$ or the phosphomimic MYB36$^{\text{DDD}}$, both of which fully complement CASP1 domain fusion (Fig. 3a and Supplementary Table 2). The fusion defects exhibited by MYB36$^{\text{AAA}}$ can be described as a band of 'speckles' roughly aligned with the endodermis central plane (Fig. 3b). These CASP1 speckles consist of many smaller disconnected patches, in comparison with the larger, more connected domains caused by the loss of SGN3 signalling in *sgn3* or *cif1 cif2* (Fig. 3a–c and Extended Data Fig. 3c). As expected, the ability to fuse CASP1 domains correlates with the formation of a continuous CS lignin (Fig. 3b) and early formation of a diffusion barrier (Fig. 3d).

Importantly, we found that the domain fusion defect in *myb36* MYB36$^{\text{AAA}}$ is resistant to external CIF2 application (Fig. 3b,c and Extended Data Fig. 3c,d), suggesting that CIF2-induced domain fusion is impaired by the absence of functional phospho-sites in MYB36 (Fig. 3f middle). By contrast, CIF2-induced ectopic lignification is unaffected by MYB36$^{\text{AAA}}$, since ectopic lignin in *myb36* MYB36$^{\text{AAA}}$ is further enhanced by external CIF2 application (Fig. 3b). Accordingly, *myb36* MYB36$^{\text{AAA}}$ has a delayed PI block, similar to untransformed *myb36* (Fig. 3d).

Our data strongly suggest that the SGN3 pathway operates through multiple branches, one requiring MYB36 activation for CASP domain fusion, probably via MPK phosphorylation, and another triggering compensatory ectopic lignification independent of MYB36 (Fig. 3f left). Specificity could thus arise from the FLS2 pathway's inability to activate MYB36.

We also found that different C-terminal tags affect the functionality of MYB36$^{\text{AAA}}$, with large tags such as Turbo-GFP (847 aa) and mCherry (406 aa) apparently enhancing functionality of all MYB36 variants compared with their untagged version (Fig. 3d and Supplementary Table 2), possibly due to enhanced stability. Nevertheless, despite similar accumulation levels, MYB36$^{\text{AAA}}$-mCherry was still unable to fully complement CASP domain fusion in *myb36*, unlike the other variants (Extended Data Fig. 3b).

The phosphomimic MYB36$^{\text{DDD}}$ could fully complement CASP domain fusion and CS barrier function in *myb36*, comparable to MYB36$^{\text{WT}}$ (Fig. 3a–d). Interestingly, the untagged MYB36$^{\text{DDD}}$ shows gain-of-function activity, improving CASP domain fusion in *sgn3*, whereas MYB36$^{\text{AAA}}$ could not (Fig. 3e,f right). This further supports the idea that the predicted MPK phospho-sites in MYB36 are essential for CASP domain fusion induced by the SGN3 pathway. Furthermore, MYB36 protein accumulation and stability appear to be important determinants of its activity within the SGN3 pathway.

Multiple MPKs contribute to CS integrity in the SGN3 pathway

MPKs are direct, key regulators of transcription factors, and our data indicate their potential in directly regulating MYB36 activity. Yet, several MPKs are reported to be activated by both SGN3 (ref. 20) and FLS2 pathways[27,40]. In *2-in-Endo* seedling roots, we confirmed that both pathways can activate MPK3 and MPK6 in the endodermis upon flg22 or CIF2 treatments (Fig. 4a). To obtain a more global picture of MPK activities in the endodermis, we generated an expression atlas for all 20 MPKs in *Arabidopsis* (Supplementary Table 3) by generating and analysing individual transcriptional fluorescent marker lines. Overall, we observed broad expression patterns across different tissues (Supplementary Table 3). We found that at least 12 MPKs are expressed in the endodermis, hence a subset could easily transduce specific signals downstream of SGN3 and FLS2 (Extended Data Fig. 4b,c). Integrating our atlas with RNA-seq[30] and translating ribosomal affinity purification (TRAP) data enriched in the endodermal cell file (Extended Data Fig. 4a), we homed in on 8 candidates (*MPK2/3/6/9/15/16/17/19*). However, none of the tested *mpk* single mutants show strong defects in CS barrier function or CASP1 domain fusion (Fig. 4b and Extended Data Fig. 5a). We nevertheless observed a slight delay in forming a diffusion barrier in *mpk2* (Fig. 4b), fitting with the in vitro phosphorylation data of MYB36 being a substrate for MPK2, 3 and 16 (ref. 39). However, no obvious discontinuities persist at maturity in *mpk2* CASP1-GFP (Extended Data Fig. 5a). Moreover, neither T-DNA nor CRISPR *mpk2 mpk16* double mutants showed a significant barrier diffusion or CASP1-GFP defect (Fig. 4b and Extended Data Fig. 5a,c), suggesting that higher-order mutants will be required for observing strong and reliable CS formation phenotypes.

Because MPKs are involved in many processes, dissecting their function without pleiotropic effects in higher-order mutants is challenging. To circumvent this problem, several alternative tools were tested. First, we expressed HopAI1, a *Pseudomonas syringae* effector that specifically deactivates multiple MPKs, including MPK3/4/6 (refs. 41–43), under an endodermis-specific estradiol (EST) inducible promoter (*pLTPG15::XVE>>pLexA::HopAI1*, hereafter indHopAI1). HopAI1 induction in wild type leads to delayed barrier formation and some ectopic lignin, suggesting that MPK activities are required for CS functionality. No phenotype is observed using an inactive HopAI1$^{\text{H103A}}$ mutant (Fig. 4c and Extended Data Fig. 4d). However, at our confocal resolution, HopAI1 induction does not seem to affect CASP domain fusion (Extended Data Fig. 4d).

Since *mpk3 mpk6* double mutants are embryo lethal[44], we used conditional loss-of-function lines expressing *pMPK3::MPK3*^{TG} or *pMPK6::MPK6*^{YG} in an *mpk3 mpk6* background[45,46]. MPK3$^{\text{TG}}$ and MPK6$^{\text{YG}}$ are specifically sensitive to NM-PP1, a bulky analogue of the general kinase inhibitor PP1. Indeed, 1-day inhibitor treatment of these lines delayed the PI block without causing other developmental defects (Fig. 4d).

Fig. 3 | Predicted phospho-sites of MYB36 important for SGN3-dependent CS domain fusion. a, CASP1-GFP (gradient intensity) in *myb36* CASP1-GFP transformed with untagged MYB36 genomic DNA constructs: ^{WT}, *MYB36*^{AAA} (S18A, S146A, S169A), *MYB36*^{DDD} (S18D, S146D, S169D). T2 roots at mature CS stage (16th–17th cell) are shown. Untransformed *myb36*, *wild type* and *sgn3* with CASP1-GFP are shown as controls. For T1 phenotype distribution, see Supplementary Table 2. Colour bar shows gradient intensity of GFP. **b**, CS and CASP1 domain fusion in *myb36* transformed with untagged *MYB36* variants after 1 d of 1 µM CIF2 or H_2O treatment. Endodermal cell surface views at mature CS stage (16th–17th cell) show CASP1-GFP (C, green), lignin (L, magenta) and overlaps of the two channels (Merged). Arrowheads show ectopic lignin on cortex-facing side. Scale bars, 5 µm. **c**, Quantification of CASP1 domain properties: number of CASP1-GFP fragments per 100 µm in surface views. *myb36* CASP1-GFP transformed with untagged *MYB36*^{WT} (WT), *MYB36*^{AAA} (AAA) or *MYB36*^{DDD} (DDD) are treated for 1 d with H_2O (grey) and 1 µM CIF2 (pink) ($n \geq 10$). For fragment size, see Supplementary Fig. 3c. **d**, PI penetration assay quantifies CS barrier function of *myb36* CASP1-GFP transformed with *MYB36* constructs (WT, AAA, DDD), untagged or with C-terminal mCherry or Turbo-GFP tag (short for 6xHis3xFLAG-TurboID-GFP) (T1 roots, $n \geq 10$). Multiple comparisons were done separately for each tag group, always including 2 controls and 3 lines per tag group. **e**, Quantification of CS discontinuity of *sgn3 CASP1-GFP* transformed with untagged *MYB36*^{WT}, *MYB36*^{AAA} or *MYB36*^{DDD} (T1 and untransformed; $n \geq 8$). **f**, Schematic of working models. SGN3 signalling acts through MYB36, possibly by boosting phosphorylation, to promote CASP domain fusion. Ectopic lignin is induced by SGN3 signalling independently of MYB36; MYB36$^{\text{AAA}}$ is sufficiently active to induce CASP domain islands. MYB36$^{\text{AAA}}$ cannot mediate CIF2-stimulated domain fusion but can mediate CIF2-stimulated ectopic lignin and acts via an unknown transcription factor (TFx); MYB36$^{\text{DDD}}$ is able to enhance CASP domain fusion without the SGN3 pathway. All data from roots at mature CS stage (16th–17th cell). For **c**–**e**, groups with the same letter are not significantly different ($P < 0.05$, one-way ANOVA and Tukey's HSD test). Untrans, untransformed.

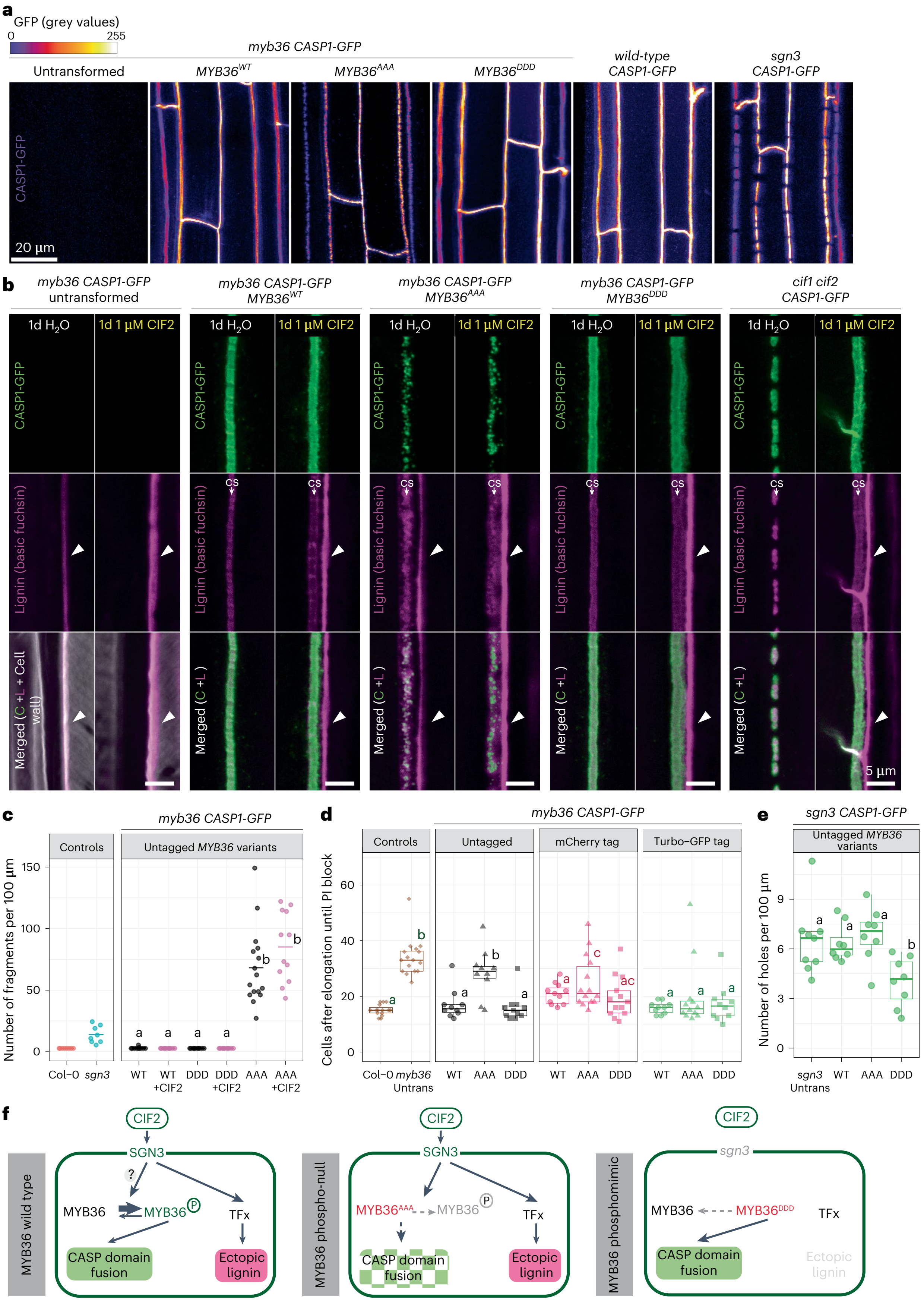
a
GFP (grey values)
0
255
myb36 CASP1-GFP
Untransformed
$MYB36^{WT}$
$MYB36^{AAA}$
$MYB36^{DDD}$
wild-type CASP1-GFP
sgn3 CASP1-GFP
CASP1-GFP
20 µm
b
myb36 CASP1-GFP untransformed
myb36 CASP1-GFP $MYB36^{WT}$
myb36 CASP1-GFP $MYB36^{AAA}$
myb36 CASP1-GFP $MYB36^{DDD}$
cif1 cif2 CASP1-GFP
1d H_2O
1d 1 µM CIF2
CASP1-GFP
Lignin (basic fuchsin)
CS
Merged (C + L + Cell wall)
Merged (C + L)
5 µm
c
myb36 CASP1-GFP
Controls
Untagged MYB36 variants
Number of fragments per 100 µm
0
50
100
150
a
b
Col-0
sgn3
WT
WT +CIF2
DDD
DDD +CIF2
AAA
AAA +CIF2
d
myb36 CASP1-GFP
Controls
Untagged
mCherry tag
Turbo–GFP tag
Cells after elongation until PI block
0
20
40
60
a
b
c
ac
Col-0
myb36 Untrans
WT
AAA
DDD
e
sgn3 CASP1-GFP
Untagged MYB36 variants
Number of holes per 100 µm
0
3
6
9
a
b
sgn3 Untrans
WT
AAA
DDD
f
MYB36 wild type
CIF2
SGN3
?
MYB36
MYB36
P
TFx
CASP domain fusion
Ectopic lignin
MYB36 phospho-null
CIF2
SGN3
$MYB36^{AAA}$
MYB36
P
TFx
CASP domain fusion
Ectopic lignin
MYB36 phosphomimic
CIF2
sgn3
MYB36
$MYB36^{DDD}$
TFx
CASP domain fusion
Ectopic lignin

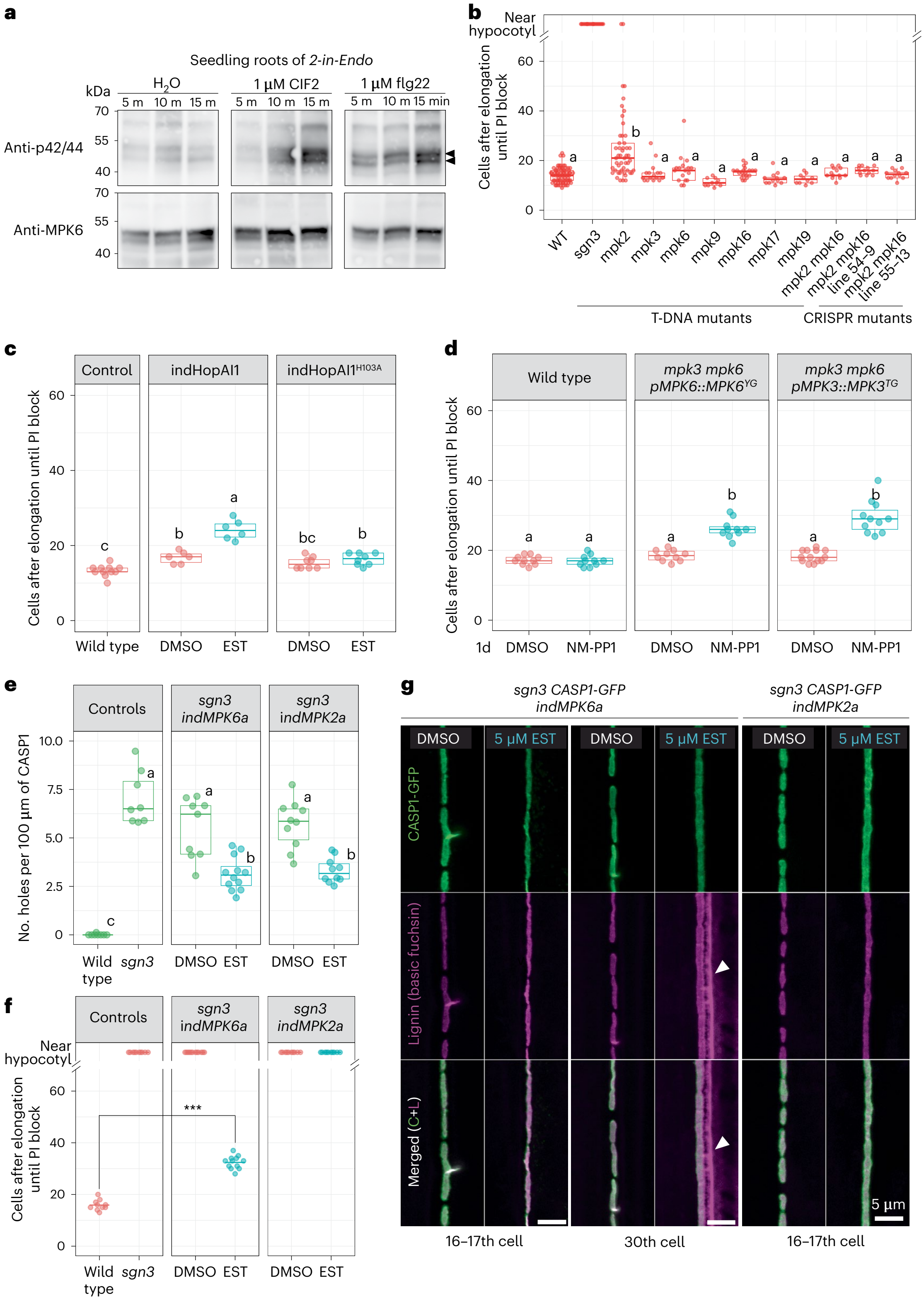

We also used a gain-of-function approach to investigate whether constitutively active MPK6a and MPK2a can alleviate CS defects in *sgn3*. We found that expressing MPK6a or MPK2a under an inducible endodermis-specific promoter (ind) in *sgn3* reduces CASP1 domain discontinuities at maturity (Fig. 4e). Interestingly, only induction of MPK6a, but not MPK2a, partially restores the diffusion barrier in *sgn3* (Fig. 4f and Extended Data Fig. 5b). This correlates with MPK6a activating ectopic ROS and ectopic lignin and suberin formation in *sgn3*, in contrast to MPK2a (Fig. 4g, and Extended Data Figs. 4e,f, and 7d). MPK6a thus appears to have a broader activity, affecting specific and common branches of the SGN3 pathway, while MPK2a contributes more specifically to CASP domain fusion.

Since MPK6a is sufficient to induce ectopic lignin in *sgn3*, we investigated whether MPK6 is necessary for SGN3-dependent ectopic lignification by testing whether CIF2-induced ectopic lignin is affected in *mpk6*. We found that 1-day CIF2 treatment could induce similarly strong ectopic lignin in *mpk6* and wild type, as well as in *mpk3* (Extended Data Fig. 4g). This suggests that genes in addition to MPK6 must contribute

Fig. 4 | Multiple MPKs contribute to CS integrity in the SGN3 pathway. **a**, Immunoblots (IB) against p42/44 (phosphorylated MAPKs) indicate sizes corresponding to phosphorylated MPK6 (top arrowhead) and MPK3 (bottom arrowhead). *2-in-Endo* seedling roots treated with H_2O, 1 µM CIF2 or flg22 for 5, 10 and 15 min. Loading controls: IBs with anti-MPK6 antibody. See Source Data Supplementary Fig. 7a for original blots, Source Data Supplementary Fig. 7b for IBs on whole seedlings of *2-in-Endo* with Ponceau S as loading control and Source Data Supplementary Fig. 7c with anti-MPK6 with *mpk6* as negative control. This experiment was repeated twice with similar results. **b**, PI penetration assay quantifies CS barrier function in various *mpk* T-DNA mutants and *mpk2 mpk6* CRISPR mutants ($10 \le n \le 49$) compared to wild type ($n = 73$) and *sgn3* ($n = 10$). Data from multiple independent experiments are combined. Unbalanced Tukey's HSD test for unequal replication. See Extended Data Fig. 5c for allele description of the two CRISPR mutant lines. **c**, PI penetration assay with endodermal suppression of multiple MPK activities by inducing HopAI1 vs inactive $\text{HopAI}^{\text{H103A}}$ in wild type ($n \ge 6$). Endodermis-specific estradiol (EST) inducible promoter: *pLTPG15::XVE»pLexA::HopAI1* (indHopAI1). **d**, PI penetration assay upon conditional loss of function of both MPK3 and MPK6 ($n \ge 10$). *pMPK6::MPK6*^{YG} or *pMPK3::MPK3*^{TG} are sensitive to NM-PP1 in *mpk3 mpk6* background. Seedling roots (4-day-old) transferred to 5 µM NM-PP1 or DMSO for 1 d. **e**, Quantification of CS discontinuity upon endodermal induction of constitutively active MPK6a or MPK2a in *sgn3 CASP1-GFP* ($n \ge 8$). **f**, PI penetration assay upon endodermal induction of MPK6a or MPK2a in *sgn3 CASP1-GFP*. Two-sided Welch's *t*-test compares indMPK6a ($n = 12$) to the wild type ($n = 10$), $^{***}P = 5.72 \times 10^{-14}$. **g**, CS lignin and CASP1 phenotypes upon endodermal induction of MPK6a or MPK2a in *sgn3 CASP1-GFP* at 16th–17th and 30th endodermal cells after onset of elongation. Surface views show CASP1-GFP (C, green) and lignin (L, magenta). Arrowheads show ectopic lignin on cortex-facing side. Scale bars, 5 µm. For **b**–**e**, groups with the same letter are not significantly different ($P < 0.05$, one-way ANOVA and Tukey's HSD). 'ind' designates 'pLTPG15::XVE»pLexA::'. For EST induction, all seedlings were grown for 5 d on 5 µM EST or DMSO non-induced control before analysis. Whiskers indicate maximum and minimum values, except outliers (defined as >1.5× interquartile range above 3rd quartile or below 1st quartile, respectively).

to ectopic lignification downstream of the SGN3 pathway. Despite MPK2a and MPK6a contributing to domain growth and fusion, neither alone is sufficient to complete CS fusion. Therefore, a combination of different MPK activities appears to contribute to the three-branched outputs of the SGN3 pathway, some unique and some overlapping with the FLS2 pathway.

Activation of individual MKKs in the endodermis produces distinct outputs

Arabidopsis contains 80 MAPKKKs and 20 MAPKs, but only 10 MKKs, the direct upstream regulators of MPKs[47,48]. MKKs thus represent the narrowest part of the hourglass and the most critical step for information transfer. MKKs tend to selectively activate certain MPK combinations[39,49], suggesting that the activation of different MKKs may translate into distinct combinations of MPK activities, depending on the specific pathway triggered.

Given the relatively small number of MKKs, it is feasible to conduct a comprehensive examination of their activities in the endodermis. Since we did not find even weak phenotypes in any of the single and double mutants tested (Extended Data Fig. 7e,f,g), we decided to use our endodermal-specific induction system and introduced all 10 constitutively active MKKs in the *sgn3* background (designated indMKK1a–indMKK10a). The 10 MKKs are classified into phylogenetic groups (A–D)[47] (Fig. 5a) and interestingly, these groupings match strikingly well with the functional outcomes we observe in the endodermis.

For Group A/B members, namely MKK1/2/6/3, we found that induction of each individual MKKa in the *sgn3* endodermis can improve CASP1 and CS lignin fusion (Fig. 5b,c), although none is sufficient to rescue the barrier defects of *sgn3* in the diffusion assay (Fig. 5e). This can be attributed to the persistence of small gaps in the CS after induction (Fig. 5b), coupled with the fact that these activated variants do not induce compensatory ectopic lignin or ROS (Fig. 5b and Extended Data Fig. 7c,d). Intriguingly, unlike MPK6a, which triggers early excess suberin, MKK1/2/3a induction suppresses suberization in *sgn3* roots (Extended Data Fig. 7a). Our findings suggest that MKK1/2/3/6 are involved in transducing the SGN3-specific branch of CS domain fusion, which aligns nicely with in vitro data of MKK1-MPK2 and MKK2-MPK2 phosphorylating MYB36 (ref. 39). This fits our hypothetical model, whereby distinct SGN3 and FLS2 outputs are defined by differential regulation of MYB36 via specific MKK-MPK signalling routes (Fig. 7)[46].

Group C members MKK4 and MKK5 show broader activities. Induction of MKK4a can moderately improve domain fusion in *sgn3* (Fig. 5c) but uniquely promotes ectopic lignin and ROS production, even in the absence of SGN3 signalling (Fig. 5b and Extended Data Fig. 7c,d). This ectopic lignin is sufficient to form a delayed diffusion barrier in contrast to no barrier with non-induced control in *indMKK4a sgn3* (Fig. 5e). In addition, indMKK4a triggers early excess suberin accumulation (fluorol yellow staining) and suberin synthesis (GPAT5 expression marker) in *sgn3* (Extended Data Fig. 7a,b). These data suggest that MKK4a mediates the compensatory branches of the SGN3 pathway (ectopic lignin and excess suberin), a function akin to MPK6a's effects. Given that MKK4-MPK6 is activated by FLS2 for immune function[27,50], this cascade could regulate the common downstream outputs of both SGN3 and FLS2 in the endodermis (Fig. 7). MKK5, often considered functionally redundantly with MKK4 in immune signalling[27], has little effect on CASP1 domain fusion or ectopic lignification (Fig. 5b,c,e) but does slightly enhance suberin synthesis upon induction in the *sgn3* endodermis (Extended Data Fig. 7a,b).

Among Group D members, MKK9 stands out as we found that the others (MKK7/8/10) are either absent or only weakly expressed in the root endodermis (Extended Data Fig. 6a)[30]. Strikingly, EST induction of MKK7a and MKK9a in *sgn3* suppresses both CASP1 and CS lignin accumulation (Fig. 5b,d and Extended Data Fig. 6b,e). Electron microscopy confirms that MKK9a also abolishes ROS accumulation and membrane attachment, typical of a functional CS structure (Extended Data Fig. 7c). This suppression remains prominent in wild-type background with SGN3 present (Fig. 5d and Extended Data Fig. 6c). In wild type, MKK9a suppresses CASP1 accumulation and domain fusion but does not suppress ectopic lignification (Extended Data Fig. 6c), explaining the partial PI block phenotype (Fig. 5f and Extended Data Fig. 6f).

Fig. 5 | Activation of individual MKKs in the endodermis produces distinct outputs. **a**, MKKs 1–10 from *Arabidopsis thaliana* are classified into 4 phylogenetic groups using full length sequence[47]. **b**, CASP1 and lignin phenotypes upon endodermal induction of constitutively active MKK1–10a in *sgn3 CASP1-GFP* at 16th–17th cell. Endodermal cell surface views show CASP1-GFP (green) and lignin (magenta). Arrowheads show ectopic lignin on cortex-facing side. Scale bars, 5 µm. **c**, Quantification of CS continuity upon endodermal induction of MKK1–10a in *sgn3 CASP1-GFP* ($n \ge 11$). **d**, Quantification of CS coverage upon induction of MKK7a and MKK9a in wild type and *sgn3 CASP1-GFP* ($n \ge 10$). At mature CS stage, total CASP1 length of each overview image measured normalized to the average CASP1-GFP length in wild type to calculate percentage of CS coverage for each data point. **e**, PI penetration assay quantifies CS barrier function upon endodermal induction of MKK1–10a in *sgn3 CASP1-GFP* ($n \ge 10$). **f**, PI penetration assay upon endodermal induction of MKK9a in wild-type CASP1-GFP and in *sgn3 CASP1-GFP* ($n \ge 10$). See Extended Data Fig. 6f for T1 data and statistics. For **c**–**e**, two-sided Welch's *t*-test compares DMSO with EST for each genotype, *P* values were adjusted for multiple comparisons by Bonferroni correction ($^{***}P < 0.001$, $^{**}P < 0.01$, $^{*}P < 0.05$). For EST induction, all seedlings were grown for 5 d on 5 µM EST or DMSO. For each indMKKa genotype, two independent T2-line data are combined in **c**–**f**. Whiskers indicate maximum and minimum values, except outliers (defined as >1.5× interquartile range above 3rd quartile or below 1st quartile, respectively). Ctrls, controls.

MKK9a also has a potent inhibitory effect on suberin in *sgn3* (Extended Data Fig. 7b,c), consistent with MKK9's recognized role in ethylene signalling[51,52] and the known inhibitory effect of ethylene activation on suberin in the endodermis[53]. The other Group D members, MKK8a and MKK10a, improve CASP1 domain fusion, but not diffusion barrier defects, resembling the action of Group A/B members (Extended Data Fig. 5c,e)[54,55]. Western blot analysis confirms the enhanced accumulations of MKK1–10a upon EST induction (Extended Data Fig. 6d).

In summary, our systematic analysis of all 10 MKKs in a single cell-type demonstrates that activation of individual MKKs in the

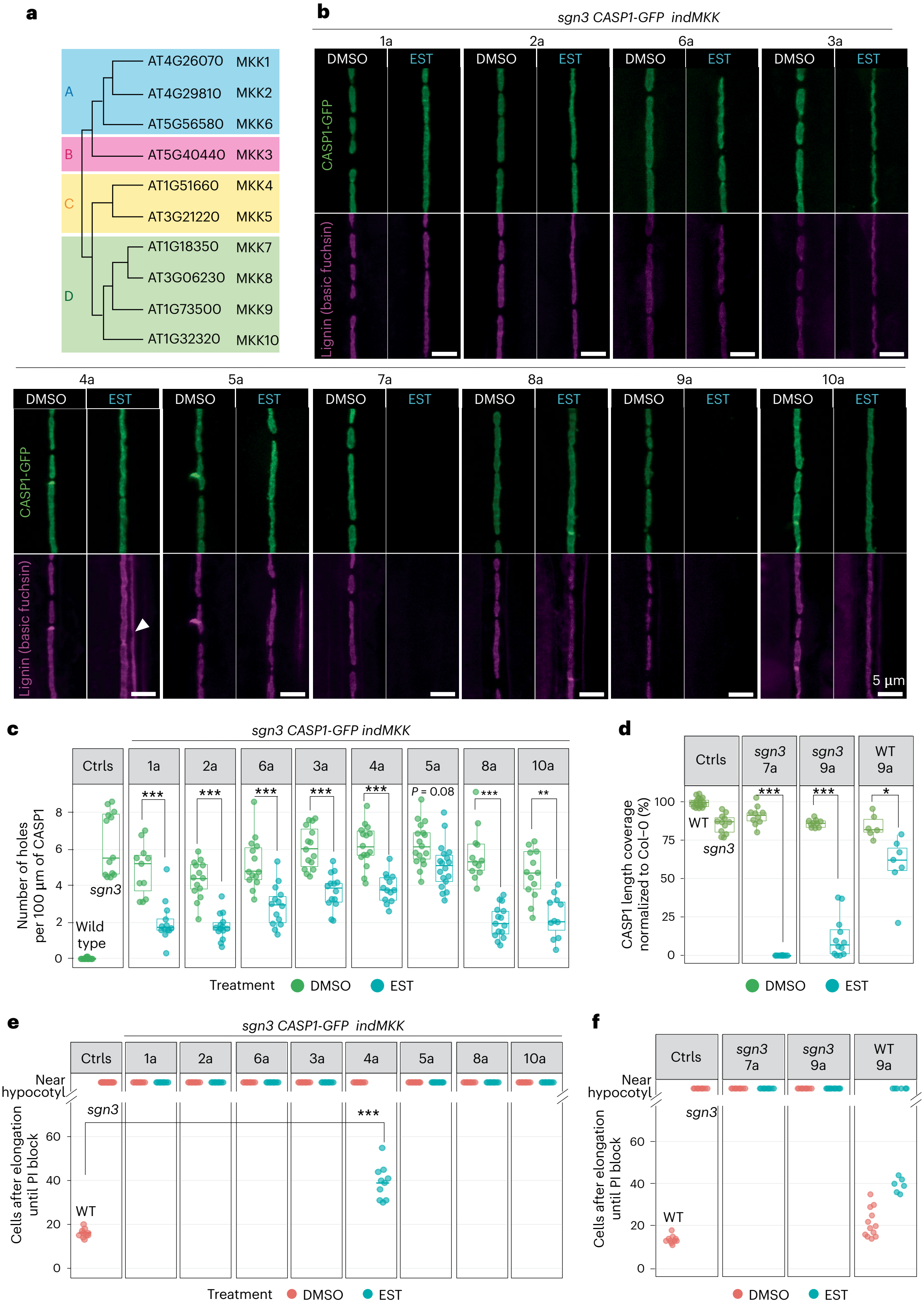

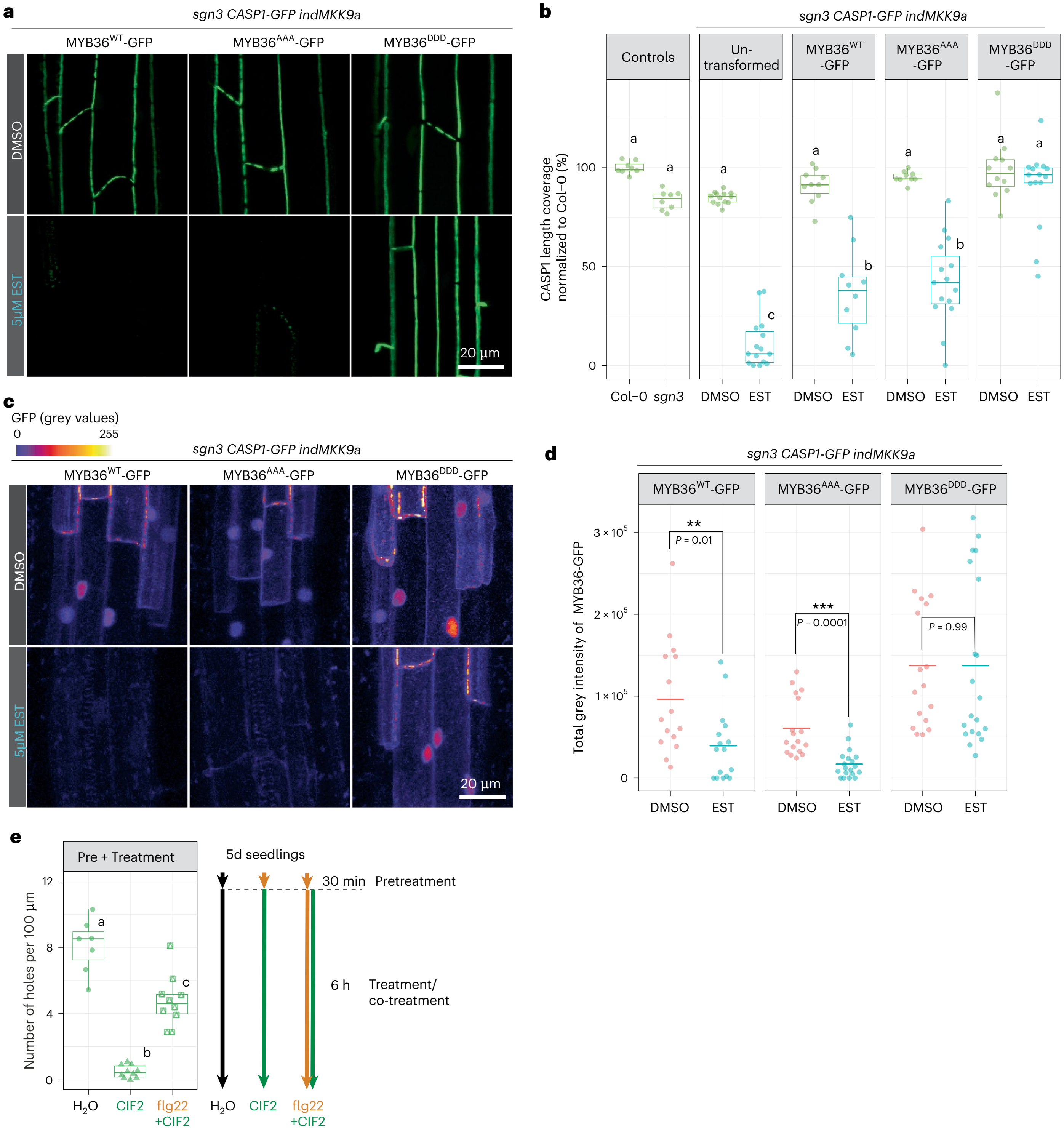

Fig. 6 | Constitutively active MKK9 inhibits CS formation via suppressing MYB36. a, CASP1-GFP phenotypes of *sgn3 CASP1-GFP indMKK9a* (T3) transformed with Turbo-GFP-tagged MYB36^{WT}-GFP, MYB36^{AAA}-GFP and MYB36^{DDD}-GFP. T2 roots at mature CS stage (16th–17th cell) are shown. **b**, Quantification of CS coverage upon induction of MKK9a *sgn3 CASP1-GFP* transformed with MYB36-GFP variants (T2, $n \geq 8$). Groups with the same letter are not significantly different ($P < 0.05$, one-way ANOVA and Tukey's HSD). **c**, Stability of MYB36 variants in *sgn3 CASP1-GFP indMKK9a* background with or without EST induction. Nuclei signals of MYB36-GFP at 7th–8th cell (start of CASP1-GFP deposition) corresponding to **a** are shown. CASP1-GFP and MYB36-GFP signals can be distinguished on the basis of different subcellular location. Colour bar shows gradient density of GFP. **d**, Quantification of MYB36 variants stability as in **c**, showing total grey intensity of nuclei signal (MYB36-GFP fluorescence) with or without EST induction at 7th–8th cell (T2, $n \geq 15$). Two-sided Welch's *t*-tests compare EST and DMSO for each genotype (***$P \leq 0.001$, **$P \leq 0.01$). For EST induction, all seedlings were grown for 5 d on 5 μM EST or DMSO before analysis. **e**, Quantification of CS continuity of *2-in-Endo CASP1-GFP* upon 30 min, 1 μM flg22 pre-treatment plus 6 h, 100 nM CIF2 treatment or 100 nM CIF2 + 1 μM flg22 co-treatment ('Pre + Treatment', $n \geq 10$). H_2O treatments were used as controls. Groups with the same letter are not significantly different ($P < 0.05$, one-way ANOVA and Tukey's HSD). For **b**, **d**, **e** boxplots, the whiskers indicate maximum and minimum values, except outliers (defined as >1.5× interquartile range above 3rd quartile or below 1st quartile, respectively).

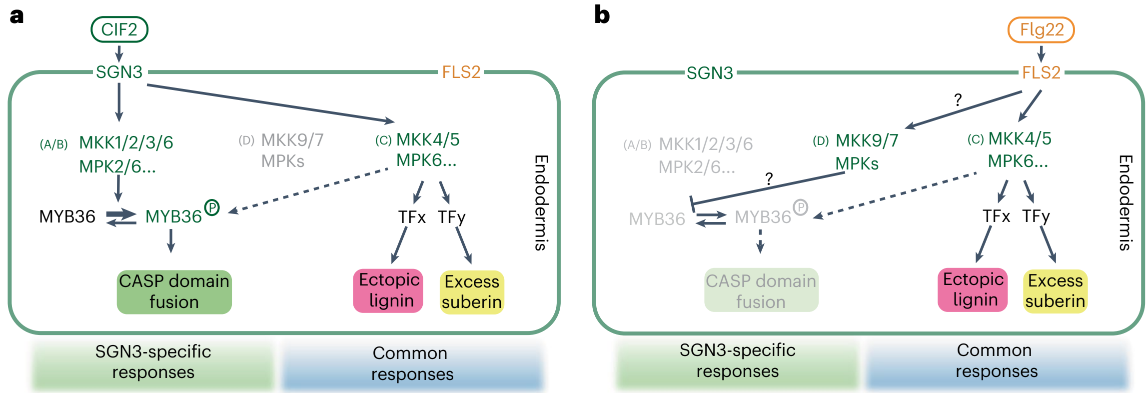

Fig. 7 | Hypothetical model of two receptor pathways in a single cell-type. a,**b**, Hypothetical model of mechanisms underlying specificity of SGN3 signalling (**a**) and FLS2 signalling (**b**) in the endodermis based on current understanding.

endodermis leads to clearly distinct output patterns. These patterns match both the common and specific outputs upon SGN3 and FLS2 stimulation in the endodermis. The Groups A/B (MKK1/2/3/6) are strong positive regulators specific to domain fusion; Group C MKK4 is the only one capable of promoting ectopic lignin and excess suberin. Finally, among Group D, MKK7 and MKK9 are strong negative regulators capable of suppressing CS development.

Constitutively active MKK9 inhibits CS formation via suppression of MYB36

The specific impact of MKK9 activation on CASP1 accumulation and fusion suggests that it could be a powerful suppressor of MYB36 activity. We tested this by introducing MYB36^{WT}, MYB36^{AAA} or MYB36^{DDD} tagged with GFP-TurboID (here labelled -GFP) into the *sgn3 indMKK9a* background (Fig. 3d and Supplementary Table 2). With MYB36^{WT}-GFP or MYB36^{AAA}-GFP, indMKK9a still suppresses CASP1 accumulation in *sgn3* (Fig. 6a,b). The phosphomimic MYB36^{DDD}-GFP, by contrast, abolishes the inhibitory effect of indMKK9a on CASP1 accumulation (Fig. 6a,b). This indicates that MKK9 suppression is conditioned by the phosphorylation status of MYB36.

We found that MKK9a induction reduces accumulation of MYB36^{WT}-GFP and MYB36^{AAA}-GFP in endodermal nuclei (Fig. 6c,d), and MYB36 levels correspond closely to the extent of CS suppression (Fig. 6a,c and Extended Data Fig. 8a). Conversely, MYB36^{DDD}-GFP levels were unaffected by MKK9a induction, and MYB36^{DDD}-GFP levels positively correlated with the rescue activity (Fig. 6 and Extended Data Fig. 8a,b). MKK9 signalling thus appears to destabilize wild type and the phospho-null variant of MYB36 to suppress its function. Intriguingly, in *sgn3 indMKK9a* lines expressing high levels of MYB36^{DDD}-GFP, we could observe ectopic CASP1 patches outside of the CSD (Extended Data Fig. 8a), mimicking hyperstimulation of the SGN3 pathway[12]. We conclude that the phosphomimic variant of MYB36 not only has an ability to complement the *sgn3* phenotype, but also reiterates SGN3 hyperstimulation, firmly placing phosphorylated MYB36 as an important downstream player of the SGN3 pathway.

The FLS2 pathway intertwines closely with ethylene signalling[54–56] known to activate MKK1/3/9[51,52,57], and MKK7 was found to contribute to flg22-induced ROS burst[58]. Hypothetically, an activation of MKK9 (and/or MKK7) by the FLS2 pathway could account for the inability of flg22 stimulation to induce closure of CS domains by negatively regulating MYB36. This negative regulation could influence the activation from positive regulators of MYB36 activity and thus exacerbate the difference between SGN3 and FLS2 signalling outputs. If this were the case, flg22-FLS2 signalling should be able to interfere with CIF2-SGN3 signalling when simultaneously activated in the same cell. Indeed, we found that pre/co-treatment of flg22 with CIF2 leads to suppression of CIF2-induced CASP1 domain fusion in 2-*in*-*Endo* (Fig. 6e), lending support to such a model (Fig. 7b).

Discussion

Signalling specificity is maintained at single-cell level

The complexity and intricacy of cellular signalling are increasingly recognized in plants[59,60]. Understanding the signalling dynamics at single-cell level is fundamental for delineating overall organismal responses. To enable both stimulation and observation of pathway activities at single-cell resolution, we utilized the unique characteristics of the SGN3 pathway, allowing for precise and quantifiable readouts in a non-dividing, easily observable cell.

Our study underlines the importance of examining signalling specificity beyond the constraints of tissue specificity and compartmentalization. We demonstrated that the FLS2 pathway in the endodermis could not substitute the SGN3 pathway in establishing a continuous Casparian strip (Fig. 1). This pertains to endogenous signalling, since the endodermis has the inherent capacity for FLS2 immune signalling[31].

SGN3 as a neo-functionalized immune receptor?

A simplistic approach to achieve specificity at single-cell level would be to have dedicated sets of receptors, signalling components and transcription factors that are insulated between one pathway and another in the same cell. However, evolution appears to have favoured a more elegant solution—reusing key signalling components from diverse processes, a common theme among multicellular organisms[61,62].

In plants, despite the expansion of the receptor repertoire for detecting a growing number of specific inputs, intracellular signalling pathways share striking similarities in their structure and components. It is thus reasonable to believe that outputs of many pathways share a common core. This is supported by the extensive interconnections among plant hormonal pathways[63] and the substantial overlaps observed in transcriptomic responses to biotic and abiotic stresses[64–66]. Our data expand this idea and show that stimulation of a developmental and an immunity receptor kinase pathway can induce common ROS, lignin and suberin production (Fig. 1). This is corroborated by transcriptional profiles, showing matching induction patterns for genes involved in lignin and suberin biosynthesis following either CIF2 or flg22 treatments (Fig. 2). These commonalities raise an intriguing question: Could both pathways have originated from a shared signalling pathway module, having diverged over time to perceive distinct inputs while maintaining partially overlapping outputs? This fits the prevalent view of plant evolution being driven by cycles of gene duplication and neo-functionalization[67]. Once plants developed a mechanism for ROS production and lignification during defence, they may have adapted these responses for more precise developmental purposes, leading to the emergence of the primary function of the present-day SGN3 pathway, possibly through initially subtle divergences in the substrate specificity of the receptor kinase domains.

Intriguingly, our comparative RNA-seq analysis revealed substantial overlaps among early, highly responsive genes between the two pathways. Yet, despite this remarkable overlap, the FLS2 immune receptor kinase cannot replicate the central developmental function of the SGN3 pathway.

Combinatorial activation of MPK cascades can encode specific signalling outcomes

There is a remarkable potential for the combinatorial activation of kinases to encode signalling specificity in plants. Beyond the members of the MPK cascade, other extended kinase families, including several families of calcium-dependent kinases (CDKs)[68], also transduce signals from LRR-RLKs. Our study focuses on the MPK cascade's potential to confer a basic level of specificity, yet we acknowledge the role of additional signalling elements such as CDKs and phospholipids in contributing to the overall output specificity. Intriguingly, plant MPK cascades by themselves already exhibit a complex web-like structure, contrasting with the simpler, more linear pathways found in yeast and mammals[62,69,70]. Their expansion in plants has enhanced their capacity to form numerous combinations of MPKKK-MKK-MPK[49,62]. While our understanding of plant MPK network interactions has been advanced through global analyses and in vitro methods[39,71–73], the mechanisms controlling specificity within these cascades remain largely unknown. MPK3 and MPK6, for example, are reported to be activated by numerous signalling pathways associated with diverse cellular functions[4,74]. Similarly, MPK1/2/7/14 are activated by various stress pathways[75,76]. This makes it challenging to understand how MPKs would mediate specific cellular responses. Our reporter expression atlas (Supplementary Table 3) and previous tissue-wide expression analyses indicate that MPKs are broadly expressed across tissues[77,78], providing potential for combinatorial action. Our *2-in-Endo* line ensures that downstream MPKs activated by both FLS2 and SGN3 pathways encounter identical sets of target proteins. This allowed us to assign the specific activity of SGN3 to its differential activation of MYB36, shown to be an MPK target in vitro[39] (Fig. 3). Other endodermis-expressed MYB transcription factors, such as MYB15 and MYB41 respectively involved in lignin and suberin production[79,80], are also reported to be phosphorylated by MPKs[81,82] and might be mediators of the pathway responses common to FLS2 and SGN3, that is, ectopic lignin and excess suberin production (Fig. 7).

In plants, MKK–MPK interactions are known to be promiscuous, which might be highly relevant for generating signalling specificity[39,49,71]. Each MKK can generate a potentially unique pattern of MPK activation; each MPK could receive inputs from different MKKs depending on the pathway involved; and individual MPKs could activate both common and unique substrates[83], suggesting an extensive interaction network. We propose that such combinatorial MPK activation patterns generate distinct 'flavours' that can drive specific outputs.

Elegant tissue-specific manipulations of MKKs in the stomatal lineage have demonstrated overlapping roles for MKKs 4/5 and 7/9 during early stages, and unique activities of MKK7/9 in late stages of stomatal development[84–86]. In addition, MKK4/5, but not MKK1/2/3/8/9, contribute to root meristem development[87]. These analyses revealed that MKKs have divergent functions over time along a complex developmental trajectory. Our simpler endodermal system uses a differentiating, non-dividing cell-type that allows distinct receptor stimulation and readouts at the same developmental stage. In our system, analysis of all ten MKKs provides compelling evidence that each MKK can activate distinct outputs within the same cell-type (Fig. 5). These functional groupings align well with MKK phylogeny and can account for both the common and unique outputs of the SGN3 and FLS2 pathways (Fig. 7).

On the basis of the matching readouts, we propose that the SGN3 pathway activates MKK1/2/3/6 (Groups A/B) to ensure domain fusion during CS development while suppressing excess suberin. Only upon strong or prolonged stimulation would the SGN3 pathway boost MKK4/5 (Group C) activity to promote ectopic lignin and excess suberin. By avoiding activation of negative regulators of CS development such as MKK9, the SGN3 pathway might further promote effective MYB36 activation. Among all MKKs, only MKK4 could enhance ROS production and lignification, consistent with a reported role of MKK4 in promoting ROS[88]. ROS homoeostasis could be achieved by balancing the activities of different MKKs downstream of SGN3, favouring CS domain closure upon low and transient stimulation, and preventing pleiotropic ectopic lignin and suberin accumulation until stronger, persistent stimulations are reached.

The FLS2 pathway in the endodermis, by contrast, might have a weaker ability to activate MKK1/2/3/6 (Groups A/B) but more potently activates MKK4/5 (Group C), leading to enhanced ectopic lignin and suberin. In addition, the inability of FLS2 to activate MYB36 may be reinforced by a stronger activation of MKK7/9, which would actively suppress MYB36 activity, fitting with the observed inhibitory effect of flg22 on CIF2 action (Fig. 6e). Previous analyses of the FLS2 pathway have painted much more complex and confusing pictures, with at least two independent MPK cascades, MKKK3/5-MKK4/5-MPK3/6 and MEKK1-MKK1/2-MPK4[27,29,89,90]. Parts of this were found to be due to perturbations of guarding resistance proteins[43,91–93].

We conclude that single cell-type analyses performed in a whole-tissue context can offer much clearer insights into signalling pathways. The complexities observed in previous studies may arise from readouts relying on protoplast experiments and/or use of total plant tissues. It is also intriguing to speculate that cells might switch between signalling states, with strong stimulation of one pathway actively suppressing another. Such dynamic modulation would allow a cell to respond to diverse stimuli, although not necessarily simultaneously.

Limitations of the study

This study provides new and conclusive evidence of divergent functional outputs of ten individual MKKs and two MPKs in a single cell-type, using a gain-of-function approach. However, future efforts require complementary loss-of-function analyses to genetically elucidate the MKK-MPK routes downstream of each pathway that lead to these distinct outputs. The major barrier is the redundancies and pleiotropic effects that arise from broad perturbation of multiple MPKs and/or MKKs. Potential workarounds, such as cell-type-specific MPK inhibition by HopAI1 phosphothreonine lyase activity, appears to be restricted to a subset of MPKs[41–43]. Future studies would benefit from testing additional approaches for precise tissue-specific MPK knockouts.

Our data support a compelling model of possible differential phosphorylation of MYB36 downstream of FLS2 and SGN3 pathways, driving output specificity. However, we have been unable to obtain sufficient amounts of MYB36 from *2-in-Endo* to determine their phosphorylation states after peptide treatment, due to the small number of responsive endodermal cells in total root cells. In planta biochemical validation of MYB36 phosphorylation would require a cell-type-specific enrichment and phosphoproteomics approach. This approach could also help confirm and further delineate the MKK-MPK network coding output specificity in the endodermis.

Methods

Plant materials

Arabidopsis thaliana ecotype Columbia (Col-0) was used as wild-type controls and the background ecotype for all experiments. The mutants *fls2* (SALK_062054C)[10], *sgn3-3* (SALK_043282)[17], *cif1 cif2*[20] (generated by CRISPR-Cas9), *myb36-2 (GK-543B11)*[19] and *pSGN3::SGN3-mVenus* in wild type[17] were previously described. The *2-in-Endo* line was generated in two steps: (1) pSGN3::FLS2-3myc-GFP was introduced into *fls2* (SALK_062054C) background and (2) *cif1 cif2* null alleles were obtained by CRISPR-Cas9 using a single sgRNA (5′-gctttggtttaggactggag-3′) that targets both genes[20,37]. The *pCASP1::FLS2-3myc-GFP fls2* (SAIL691_C04) described previously[32] was crossed with *sgn3-3* (SALK_043282) to obtain *pCASP1::FLS2-GFP fls2 sgn3*.

T-DNA mutant seeds *mpk2* (SALK_047422C)[94], *mpk3* (SALK_151594)[95], *mpk6* (SALK_073907)[95], *mpk9* (SALK_064439C), *mpk16* (SALK_059737C), *mpk17* (SALK_020801C)[96], *mpk19* (SALK_075D213C), *mkk4* (SALK_0188040C)[97], *mkk5* (SALK_047797C)[98] and *mkk9* (SAIL_60_H06)[52] were provided by the Nottingham *Arabidopsis* Stock Centre (NASC). Most T-DNA lines in our study were previously analysed and reported to show elimination of transcript/protein levels in the cited publications, with *mkk4* (SALK_0188040C) showing reduced transcript level[97]. All lines were verified for homozygosity. See Supplementary Table 4 for corresponding T-DNA screening primers. Homozygous double mutants *mpk2 mpk16* (T-DNA) and *mkk4 mkk5* (T-DNA) were generated by crossing the above indicated T-DNA mutants. *mpk2 mpk16* double mutant lines #54-9 and #55-13 were generated by CRISPR-Cas9 using MPK2-targeting sgRNA1 (5′-ccgataggccgaggcgcgta-3′) sgRNA2 (5′-tcttttgcatagttgcttcg-3′) and MPK16-targeting sgRNA1 (5′-agagtttcgagacatttacg-3′) sgRNA2 (5′- atacaccgactgcgatattc-3′). *mkk4 mkk5* (TILLING)[46,99], *mkk1* (SALK_027645)[100] *mkk2* (SAIL 511_H01)[101] and *mkk3* (SALK_051970)[102] were obtained from Jean Colcombet, while *mpk3 mpk6 pMPK6::MPK6*^{YG} and *mpk3 mpk6 pMPK3::MPK3*^{TG} were obtained from refs. 45,46.

The published constructs pCASP1::CASP1-GFP with FastRed selection cassette[36] and pGPAT5::mCitrine-SYP122 (ref. 53) were introduced into respective backgrounds by floral dipping. For pathway-specific reporters, promoter fusion constructs in Supplementary Table 2 were introduced into the *2-in-Endo* background. For the MPK expression atlas (Supplementary Table 3), promoter fusion constructs pMPK1-20::NLS-3xmVenus were introduced into wild-type background.

Plant growth conditions

Plant seeds were surface sterilized in 70% ethanol + 0.05% Tween 20 for 7–10 min, then washed in 96% ethanol and dried in sterile conditions. Seeds were stratified for 2 days at 4 °C in the dark on half-strength Murashige and Skoog (½MS) + 0.8% agar (Roth) plates containing 500 mg l^{-1} MES buffer (Duchefa). Seedlings were grown vertically for 5–6 days at 23 °C under continuous light before analysis.

Plasmid construction and plant transformation

The In-Fusion Advantage PCR Cloning kit (Clontech) and Multisite Gateway Cloning Technology (Invitrogen) were used for generation of constructs.

All inducible constructs (ind) were assembled by triple Gateway recombination reaction (LR) between entry clones P4-pELTP (LTPG15)-XVE-P1r (promoter)[103], L1-HopAI1-L2, L1-MPKa-L2 or L1-MKKa-L2 (gene of interest), and R2-3xFlag-L3 (C-terminal tag) into the destination vector pF7m34GW, containing a FastRed plant selection cassette with a 35S terminator. Complementary (c)DNA entry clones of HopAI1 and HopAI1^{H103A} were synthesized by Genscript[41]; MPK6a (D218G E222A)[104] was obtained from Jean Colcombet; MPK2a (Q188G E192A), MKK1a (T218E S224D), MKK2a (T220D T226E), MKK3a (S235E T241D), MKK4a (T224D S230E), MKK5a (T215E S221E), MKK6a (S221D T227E), MKK7a (S193E S199D), MKK8a (S195D S201E), MKK9a (S195E S201E) and MKK10a (S197E) were cloned from Col-0 cDNA and mutations obtained through site-directed mutagenesis.

All MYB36 constructs were assembled by triple Gateway recombination reaction between entry clones P4-pMYB36(4kb)-R1 (native promoter), *L1-MYB36*^{WT}*-L2*, *L1-MYB36*^{AAA}*-L2* or *L1-MYB36*^{DDD}*-L2* (gene of interest), and R2-MYB36-native terminator(250bp)-L3, R2-mCherry-4G-L3 or R2-SuperfolderGFP-TurboID(BirA*)-6His-TEV-3FLAG-L3 (terminator or C-terminal tag) into destination vectors pF7m34GW,0 containing a FastRed plant selection cassette or pFG34GW, containing a FastGreen plant selection cassette. Genomic (g)DNA entry clones of wild-type MYB36 were cloned from Col-0 gDNA, and mutants MYB36^{AAA} (S18A, S146A, S169A) and MYB36^{DDD} (S18D, S146D, S169D) were synthesized by Genscript.

The pathway-specific reporter constructs (Supplementary Table 1) and MPK reporter constructs (Supplementary Table 3) were made, first by generating promoter entry clones using In-Fusion: the endogenous promoter sequences (~2 kb before the start codon) were cloned from Col-0 gDNA or JAtY clones. The reporter constructs were then assembled by double Gateway recombination reaction between a promoter entry clone and L1-nuclear localization signal (NLS) fused to a triple mVenus fluorescent tag (3xmVenus)-L2 or L1-NLS-3xmScarlet-L2 into the destination vector pFG24GW (FastGreen), pFR7m24GW (FastRed) or pB7m24GW (BASTA selection). See Supplementary Tables 4 and 5 for plasmid and primer details.

All plasmids were transformed by heat shock into *Agrobacterium tumefaciens* GV3101 strain with pSoup plasmid (pMP90) and then transformed into the corresponding plant lines using the floral dip method[105,106]. On the basis of the plant selection marker, we typically obtained 10–30 transgenic lines for initial characterization or analyses at T1 generation. From these, 2–6 independent T2 transgenic lines were isolated for further characterization. For all T2 analysis in this paper, all plants were pre-selected using fluorescent seedling selection marker. Independent homozygous T3 lines were confirmed by non-segregation of the selection marker and used for western blot experiments or as background for further introduction of constructs. For certain experiments, T1 populations were used to fully capture the inherent expression variability due to random transformation events. This T1 analysis ensures that statistically significant phenotypic differences are indeed reflective of the constructs' effects themselves and not transgene expression variability. The use of fluorescent seed selection markers (FastRed or FastGreen)[107] substantially reduces the occurrence of false positives during our T1 and T2 selection process and facilitates our analysis without the stress of antibiotic selection.

Seedling growth and treatments

The flg22 peptide from *Pseudomonas aeruginosa* (QRLSTGSRINSAKDDAAGLQIA) was ordered from EZBioLab, and CIF2 peptide (DY*GHSSPKPKLVRPPFKLIPN, * indicates sulfated tyrosine) from Peptide Specialty Laboratories (https://www.peptid.de/). Peptides were dissolved in deionized MilliQ sterile water at the stock concentration of 1 mM and diluted in melted ½ MS agar medium to indicated concentrations. Peptide treatments: seedlings were grown vertically for 4–5 days, then transferred with care onto plates containing peptides or H$_2$O control to grow vertically for 1 day before analysis.

For time-lapse imaging and videos with peptide treatments, 3-day-old seedlings grown vertically on ½ MS plates were transferred to a hydroponic system (a 12-well Multiwell plate (CytoOne) with 6.5 ml liquid ½ MS in each well) to grow for 2 days. These 5-day-old seedlings were then transferred inside a chambered coverglass (Thermo Scientific) and then covered with a ½ MS agar block containing 1 μM peptide. A volume of 50 μl of liquid ½ MS containing the same peptide concentration was added through a channel in the middle of the agar block, directly reaching the roots.

EST (10 mM stock, Sigma, solvent dimethylsulfoxide (DMSO)) and NM-PP1 (Adipogen, solvent DMSO) were diluted to 5 μM in melted ½ MS agar medium, and 0.05% v/v DMSO was used as control treatments. For estradiol (EST) treatments, seedlings were grown vertically on EST or DMSO plates for 5 days or transferred to EST or DMSO to grow for 1 day. For NM-PP1 treatments, seedlings were grown vertically on ½ MS plates for 4 days and transferred to NM-PP1 or DMSO plates to grow vertically for 1 day.

Fluorescence microscopy

Imaging was performed using Leica SP8, Leica Stellaris or Leica Stellaris 5 WLL IR confocal laser scanning microscopes and Leica Thunder light microscope (DM6BZ). Images were taken with a ×63 water immersion objective (Leica SP8, Leica Stellaris) at zoom factor 1 for overviews and zoom factor 5 for surface views. Time-lapse images of Fig. 2f and Supplementary Videos 2 and 3 were taken with a ×63 oil immersion objective (Leica Stellaris 5 WLL IR). Time-lapse images of Extended Data Fig. 3d and Supplementary Video 1 were taken with a ×40 oil immersion objective (Leica Stellaris). Root scans for fluorol yellow (suberin staining) and pGPAT5:mCitrine-SYP122 (suberin synthesis) were acquired using a Leica Thunder light microscope with ×10 dry objective and tile-scan (10% overlap). Unless indicated otherwise, confocal images comparing genotypes/treatments were taken following the 'four identical criteria': same position in the roots, the same laser detection intensity, the same laser scanning area (zoom) and the same interval of slices for *Z*-stack projection. For overview images, maximum projection of *z*-stacks (step size = 1 µm) are shown. For surface-view images, maximum projection of *z*-stacks (step size = 0.36 µm) are shown.

The excitation and detection windows were set as follows: for live imaging, GFP (488 nm, 495–550 nm), PI (488 nm, 600–690 nm), mVenus (514 nm, 520–565nm), mCitrine (514 nm, 555–570 nm), mScarlet (561 nm, 580–640 nm) and mCherry (561 nm, 585–680 nm). For time-lapse imaging with Leica Stellaris 5 WLL IR: mVenus (507 nm, 520–560 nm) and mScarlet (555 nm, 580–600 nm). For fixed samples, sequential scanning was used to avoid interference between the following fluorescence channels: calcofluor white (405 nm, 415–435 nm), GFP (488 nm, 495–525 nm) and basic fuchsin (561 nm, 600–650 nm). For suberin analysis on Thunder: fluorol yellow (488 nm, 500–550 nm) and mCitrine (488 nm, 500–550 nm).

Propidium iodide penetration assay

PI penetration assays assess the stage of the formation of a functional CS diffusion barrier[15,16]. Seedlings were incubated in 10 µg ml^{-1} PI for 10 min and rinsed in H_2O before imaging. PI block was identified as the endodermal cell achieved the exclusion of PI signal from the inner side. The number of endodermal cells was counted from the onset of elongation until PI block. For roots with no functional barrier, PI was not blocked near the root–hypocotyl junction and roots are thus shown as individual data points in the category 'near hypocotyl' and excluded from numerical statistical tests.

Suberin quantification assay

Suberin was stained using the methanol-based fluorol yellow protocol[20,32]. Seedlings were fixed and cleared in methanol for at least 3 days at 4 °C, changing the methanol at least once. The cleared seedlings were transferred to a freshly prepared solution of Fluorol Yellow 088 (0.01% in methanol) and incubated for 1 h at room temperature or overnight at 4 °C in the dark. The stained seedlings were rinsed in methanol and transferred to a freshly prepared solution of aniline blue (0.5% in methanol) for 1 h counterstaining in the dark. Finally, the seedlings were washed briefly in water before mounting and imaging with the Leica Thunder light microscope.

Fixation and lignin staining

Fixation and staining were performed using an adapted Clearsee protocol[108,109]. Briefly, seedlings were fixed in 4% paraformaldehyde PBS solution at 4 °C overnight using 6-well or 12-well plates (CytoOne), then washed twice for 1 min with PBS. Once fixed, seedlings were cleared in Clearsee solution for at least 24 h under gentle shaking. Fixed and cleared samples were then incubated overnight in a Clearsee solution supplemented with 0.2% basic fuchsin and 0.1% calcofluor white for combined cell wall and lignin staining. Once the dye solution was removed, samples were rinsed overnight in Clearsee twice before mounting and observation using confocal microscopes.

Electron microscopy for ROS and lignin detection

Visualization of H_2O_2 (ROS) around the CS was performed with the cerium chloride assay described previously[20,37]. This detection method is based on Ce^{3+} ions reacting with H_2O_2, forming electron-dense cerium perhydroxide precipitates, which are detected by transmission electron microscopy. Briefly, seedlings were incubated in 50 mM MOPS buffer (pH 7.2) containing freshly prepared 10 mM cerium chloride ($CeCl_3$) (Sigma) for 45 min. Seedlings were then washed twice in MOPS buffer for 5 min and fixed in 2.5% glutaraldehyde solution (EMS) in 100 mM phosphate buffer (pH 7.4) for 1 h at room temperature. Then, they were postfixed in 1% osmium tetroxide (EMS) with 1.5% potassium ferrocyanide (Sigma) in phosphate buffer for 1 h at room temperature. The plants were rinsed twice in distilled water and then dehydrated in ethanol solution (Sigma) at gradient concentrations (30%, 40 min; 50%, 40 min; 70%, 40 min; 100%, 1 h ×2). This was followed by infiltration in Spurr resin (EMS) at gradient concentrations (Spurr 33% in ethanol, 4 h; Spurr 66% in ethanol, 4 h; Spurr 100%, 8 h ×2) and finally polymerized for 48 h at 60 °C in an oven. Ultrathin sections (50 nm) were cut transversally at 1.5, 2 or 3 mm from the root tip on a Leica Ultracut ultramicrotome (Leica Mikrosysteme) and picked up on a 2 × 1 mm nickel slot grid (EMS) coated with a polystyrene film (Sigma).

Visualization of lignin deposition around the CS and cell corner was done using the permanganate potassium ($KMnO_4$, Sigma) staining protocol[110,111]. The sections were post-stained with 1% $KMnO_4$ in H_2O for 45 min and rinsed several times with H_2O.

Micrographs were taken with a CM100 transmission electron microscope (FEI) at an 80 kV acceleration voltage with a TemCamF416 digital camera (TVIPS) using the software EM-MENU 4.0 (TVIPS). Panoramic views were aligned using the software IMOD[112].

Ectopic ROS quantification from EM images

For Extended Data Fig. 7d EM ROS quantification, all samples from the selected lines—indMKK2a, indMKK4a, indMPK6a and indMPK2a in *sgn3 CASP1-GFP* with and without estradiol induction were collected, prepared and imaged in a single experiment. We assessed 5 roots per sample and quantified the ROS staining patterns categorically cross an average of 42 endodermal cells per sample: from the TEM images, each endodermal cell was carefully examined for ROS staining patterns (electron-dense dots and patches) occurring outside of the Casparian strip region, typically between the endodermis–cortex boundary. These ectopic ROS patterns were categorized as no, yes low or yes strong on the basis of their intensity.

RNA-seq experiments and analysis

Sample preparation for RNA-seq experiments was as previously described[20]. Briefly, wild-type, *sgn3*, *fls2* and p*CASP1::FLS2-GFP fls2* seeds were grown vertically on a sterile mesh on solid ½ MS plates for 5 days and transferred onto fresh ½ MS solid medium containing 1 µM peptides and mock plates (mock and peptide treatments always transferred in parallel). After 30-, 120- and 480-min incubation on plates, whole roots from 2 square plates (50 ml) were cut and collected for each sample, then immediately frozen in liquid nitrogen. Three biological replicates for each sample were conducted on three different days. Total RNA was extracted with a TRIzol-adapted ReliaPrep RNA extraction kit (Promega).

Libraries were prepared by the Lausanne Genome Technology Facility following the same protocol[20]. RNA quality control was performed on a Fragment Analyzer (Advanced Analytical Technologies). Total RNA (1,000 ng) was used to prepare RNA-seq libraries with the Illumina TruSeq Stranded mRNA reagents (Illumina) on a Sciclone liquid handling robot (PerkinElmer) using a PerkinElmer-developed automated script. The resulting library was used for cluster generation with the Illumina TruSeq SR Cluster Kit v4 reagents and sequenced on the Illumina HiSeq 2500 system using TruSeq SBS Kit v4 reagents. The Illumina Pipeline Software v.2.20 was used to process sequencing data.

The Lausanne Genomic Technologies Facility performed the data processing using their in-house RNA-seq pipeline, as described in ref. 20. Briefly, purity-filtered read trimming for adapters and low-quality sequences was done with Cutadapt (v.1.8)[113] and removal of reads matching ribosomal RNA sequences with fastq_screen (v.0.11.1). Low complexity reads were filtered with reaper (v.15-065)[114]. Cleaned reads were aligned against *A. thaliana* TAIR10 genome using STAR (v.2.5.3a)[115] and read counts per gene locus were obtained with htseq-count (v.0.9.1)[116] using *A. thaliana* TAIR10 Ensembl 39 gene annotation. RSeQC (v.2.3.7)[117] was used to evaluate the quality of the data alignment.

Statistical analysis for genes was performed in R (3.5.3). Genes with low counts were filtered out according to the rule of one count per million (cpm) in at least one sample. Library sizes were scaled using trimmed mean of M values normalization and log transformed into cpm (EdgeR package v.3.24.3)[118]. Data were corrected for the experimental batch effect using the removeBatchEffect function (limma). Statistical quality controls were performed through pairwise sample correlations, clustering and sample Principal component analysis using batch corrected normalized data. Differential expression was computed using the limma-trend approach by fitting all samples into one linear model[119]. The experimental batch factor was added to the model. Two-sided moderated *t*-test was used for each pairwise comparison (peptide-treated vs H_2O-treated) per timepoint. The adjusted *P* value was computed using the Benjamini–Hochberg method, controlling for false discovery rate. To determine genes significantly regulated by CIF2 or flg22 (*s in Fig. 2 and Extended Data Fig. 2), the adjusted *P* value was set to be below 0.05 ($P_{adj} < 0.05$).

Heat maps of gene lists in Fig. 2c,d were selected on the basis of published genes involved in lignin and suberin biosynthesis[20,120]. Figure 2e genes were based on the intersection of RNA-seq datasets in ref. 30 and microarray datasets in ref. 19 that report significant downregulation in *myb36* mutants compared with wild type. *myb36* vs wild type regulation heat map (left) was generated using the data in ref. 30. Figure 2b genes were based on genes significantly upregulated by flg22 in whole seedlings[41]. The heat map of wild type treated with flg22 (left) in Extended Data Fig. 2b was generated using the data in ref. 41.

GO-enrichment analyses were performed using the clusterProfiler R package (3.18.1) with 'Biological process', and *P* value was adjusted using the Benjamini–Hochberg method with a cut-off of 0.05. GO annotations used the org.At.tair.db R package (3.12.0). Gene ratio represents the gene counts in a GO category that are differentially regulated by a pathway divided by the total number of genes in that GO category.

For Fig. 4a and Supplementary Fig. 7, seedlings were grown vertically for 5 days on sterilized mesh on solid ½ MS media. The seedlings were treated by adding 20 ml liquid ½ MS containing respective peptides or H_2O control to submerge the roots. At 5, 10 and 15 min, liquid was drained and roots were cut (Fig. 4a), or whole seedlings were collected (Source Data Supplementary Fig. 7b). For Extended Data Fig. 5b and 6d, seedlings were grown for 5–6 days on sterilized mesh on solid ½ MS media supplemented with EST or DMSO.

Root tissues collected were immediately frozen in liquid nitrogen and ground using Tissue Lyser II (Qiagen). Extraction buffer (50 mM Tris HCl pH 7.5, 150 mM NaCl, 0.5 mM EDTA, 1% Triton X-100, 50 mM β-glycerophosphate, 1 mM phenylmethylsulfonyl fluoride, 100 µM Na orthovanadate, 5 mM Na fluoride, 2.5 mM $MgCl_2$, 1x complete EDTA-free protease inhibitor cocktail) was added to the frozen samples. The samples were briefly mixed by vortexing and centrifuged at 21,000 × *g* for 15 min at 4 °C. The supernatant was transferred to new tubes and the total protein concentration was measured using the Bradford method (Thermo Fisher). After adjusting total protein concentration, the proteins were denatured by addition of 3x (v/w) NuPAGE LDS sample buffer + 10 mM dithiothreitol (Invitrogen, NP0007) and heated for 5 min at 95 °C.

Equal amounts of protein were loaded (~20–40 µg per lane) and separated on 10% or gradient (4–12%) pre-cast acrylamide gels (Eurogentec). After electrophoresis, the separated proteins were transferred onto PVDF membranes (Immobilon-E, Merck-Millipore) using Pierce FastBlotter G2 semi-dry blotting (Thermo Fisher). The blot was blocked in 1% blocking buffer in TBS (western blocking reagent, Roche) for 1 h at room temperature before incubation with primary antibodies: anti-p44/42 (1:1,000, Cell Signaling Technologies, 4370), anti-MPK6 (1:10,000, Sigma, A7104), anti-FLAG conjugated M2 peroxidase (1:500, Sigma, A8592) and anti-actin (1:2,000, Sigma, A0605) in 0.5% blocking buffer + TBS-0.05% Tween overnight at 4 °C. After washing the blot two to three times with 1x TBS + 0.1% Tween (TBS-T), the blot was treated with secondary antibodies (anti-rabbit, 1:10,000, Agrisera for anti-p44/42; anti-rabbit HRP ECL, 1:30,000 for anti-MPK6; anti-mouse HRP, 1:5,000 for actin, Promega) in 0.5% blocking buffer + TBS-0.05% Tween for 2 h and then washed 5–7 times with TBS-T. For loading control detection of MPK6 and actin, the original membrane was stripped (Thermo Scientific). Signal was detected with SuperSignal West Pico Plus and Femto kits (Thermo Scientific).

Quantification and statistical analysis

All fluorescence microscopy images were processed using Fiji (ImageJ2 v.2.9.0/1.53t) with Fiji macros to semi-automate the processing and quantification[121]. Macros will be made available on request.

Percentages (%) of gaps in CASP1-GFP (Fig. 1e and Extended Data Fig. 1h) were based on maximum projections of surface-view images (GFP channel) after thresholding to distinguish background from signal. Quantification represents the percentage of uncovered area (background) of a fused CASP1-GFP belt reconstructed from connecting individual domains using a selection Bush tool. Fully connected CASP1-GFP yields 0% of gaps.

Numbers of holes per 100 µm of CASP1-GFP (Figs. 3e, 4e, 5c, 6e and Extended Data Fig. 1c) were based on maximum projections of overviews (GFP channel) after thresholding to distinguish background from signal. Steps for quantification are detailed in Extended Data Fig. 1b. Each data point represents the average number of holes per 100 µm calculated from a single overview image.

Quantifications of total grey intensity of nuclei signals (Fig. 2f) were calculated from 'sum slice projection' of overview images at each hour. This method sums the intensity values at each pixel location throughout the stack and projects the sum onto a two-dimensional image. This is useful for visualizing the total intensity contribution from all slices in the stack, especially in the cases of overlapping nuclei. Thresholding and region of interest selection were then applied to isolate nuclei signals from noise and background. Similar procedures were used for Fig. 6d to calculate total grey intensity of MYB36 nuclei signals from maximum projection of overview images.

For quantification of CASP1 domain properties: number of fragments per 100 µm (Fig. 3c) and the average size of fragments (Extended Data Fig. 3c) were based on the same data points from maximum projections of surface-view images. Thresholding followed by particle analysis (no minimum size) was used to quantify the number of fragments and the average size of fragments in a single image. The length of CASP1 in µm for a single image was measured and used to calculate the number of fragments per 100 µm.

Quantification of CS coverage (Figs. 5d, 6b and Extended Data Fig. 6e) is represented by the percentage of CASP1 length coverage normalized to wild type. Total CASP1 length (measured after applying skeletonize (Fiji)) of each overview image (maximum projection) was measured and then normalized to the average CASP1-GFP length in wild-type roots from the same experiments to calculate the percentage of CS coverage for each data point.

All graphs and statistical analyses were performed using R 4.0.4 (http://www.R-project.org/). For multiple comparisons within the same dataset, analysis of variance (ANOVA) followed by Tukey's honestly significant difference (HSD) test was applied when linear model assumptions were met. Unbalanced Tukey's test was used for unequal replication. For comparing the mean of one sample with a control or treatment versus no treatment, Welch's *t*-test was used: for multiple comparisons using *t*-tests, *P* values were adjusted by Bonferroni correction. In boxplots, boxes span the first to third quartiles, with the bold line representing the median. Whiskers indicate maximum and minimum values, except outliers (defined as >1.5× interquartile range above the third quartile or below the first quartile, respectively). Outliers are always shown as dots. Bold lines in dot plots represent the mean. Each point in the boxplot or dot plot represents a data point from an individual root (*n*). Statistical parameters, error bars and *n* are reported in the Figure legends.

Reporting summary

Further information on research design is available in the Nature Portfolio Reporting Summary linked to this article.

Data availability

The full RNA-seq dataset is deposited at the GEO depository, accession: GSE270950. All other data are available in the article and extended data. Plasmids and transgenic plant seeds generated in this study will be made available on request, but we may require a payment and/or a completed Materials Transfer Agreement if there is potential for commercial application. Further information and requests for resources and reagents should be directed to and will be fulfilled by the lead contact, N.G. (niko.geldner@unil.ch). Source data are provided with this paper.

Code availability

This study did not generate new code. R scripts used to generate graphs or Fiji macros used for image processing and quantifications will be made available on request.

References

1. Lewis, T. S., Shapiro, P. S. & Ahn, N. G. Signal transduction through MAP kinase cascades. *Adv. Cancer Res.* **74**, 49–139 (1998).
2. Colcombet, J. & Hirt, H. *Arabidopsis* MAPKs: a complex signalling network involved in multiple biological processes. *Biochem. J.* **413**, 217–226 (2008).
3. Arthur, J. S. C. & Ley, S. C. Mitogen-activated protein kinases in innate immunity. *Nat. Rev. Immunol.* **13**, 679–692 (2013).
4. Zhang, M. & Zhang, S. Mitogen-activated protein kinase cascades in plant signaling. *J. Integr. Plant Biol.* **64**, 301–341 (2022).
5. Lehti-Shiu, M. D., Zou, C., Hanada, K. & Shiu, S.-H. Evolutionary history and stress regulation of plant receptor-like kinase/pelle genes. *Plant Physiol.* **150**, 12–26 (2009).
6. Soltabayeva, A. et al. Receptor-like kinases (LRR-RLKs) in response of plants to biotic and abiotic stresses. *Plants* **11**, 2660 (2022).
7. Liu, M. & Zen, K. Toll-Like receptors regulate the development and progression of renal diseases. *Kidney Dis.* **7**, 14–23 (2021).
8. Osumi-Sutherland, D. et al. Cell type ontologies of the Human Cell Atlas. *Nat. Cell Biol.* **23**, 1129–1135 (2021).
9. Apelt, F. et al. Shoot and root single cell sequencing reveals tissue- and daytime-specific transcriptome profiles. *Plant Physiol.* **188**, 861–878 (2021).
10. Zipfel, C. et al. Bacterial disease resistance in *Arabidopsis* through flagellin perception. *Nature* **428**, 764–767 (2004).
11. Chinchilla, D., Bauer, Z., Regenass, M., Boller, T. & Felix, G. The *Arabidopsis* receptor kinase FLS2 binds flg22 and determines the specificity of flagellin perception. *Plant Cell* **18**, 465–476 (2005).
12. Doblas, V. G. et al. Root diffusion barrier control by a vasculature-derived peptide binding to the SGN3 receptor. *Science* **355**, 280–284 (2017).
13. Nakayama, T. et al. A peptide hormone required for Casparian strip diffusion barrier formation in *Arabidopsis* roots. *Science* **355**, 284–286 (2017).
14. Barberon, M. & Geldner, N. Radial transport of nutrients: the plant root as a polarized epithelium. *Plant Physiol.* **166**, 528–537 (2014).
15. Alassimone, J., Naseer, S. & Geldner, N. A developmental framework for endodermal differentiation and polarity. *Proc. Natl Acad. Sci. USA* **107**, 5214–5219 (2010).
16. Naseer, S. et al. Casparian strip diffusion barrier in *Arabidopsis* is made of a lignin polymer without suberin. *Proc. Natl Acad. Sci. USA* **109**, 10101–10106 (2012).
17. Pfister, A. et al. A receptor-like kinase mutant with absent endodermal diffusion barrier displays selective nutrient homeostasis defects. *ELife* **3**, e03115 (2014).
18. Hosmani, P. S. et al. Dirigent domain-containing protein is part of the machinery required for formation of the lignin-based Casparian strip in the root. *Proc. Natl Acad. Sci. USA* **110**, 14498–14503 (2013).
19. Kamiya, T. et al. The MYB36 transcription factor orchestrates Casparian strip formation. *Proc. Natl Acad. Sci. USA* **112**, 10533–10538 (2015).
20. Fujita, S. et al. SCHENGEN receptor module drives localized ROS production and lignification in plant roots. *EMBO J.* **39**, e103894 (2020).
21. Schulze, B. et al. Rapid heteromerization and phosphorylation of ligand-activated plant transmembrane receptors and their associated kinase BAK1. *J. Biol. Chem.* **285**, 9444–9451 (2010).
22. Sun, Y. et al. Structural basis for flg22-induced activation of the *Arabidopsis* FLS2-BAK1 immune complex. *Science* **342**, 624–628 (2013).
23. Okuda, S. et al. Molecular mechanism for the recognition of sequence-divergent CIF peptides by the plant receptor kinases GSO1/SGN3 and GSO2. *Proc. Natl Acad. Sci. USA* **117**, 2693–2703 (2020).
24. Chinchilla, D. et al. A flagellin-induced complex of the receptor FLS2 and BAK1 initiates plant defence. *Nature* **448**, 497–500 (2007).
25. Alassimone, J. et al. Polarly localized kinase SGN1 is required for Casparian strip integrity and positioning. *Nat. Plants* **2**, 16113 (2016).
26. Lee, Y., Rubio, M. C., Alassimone, J. & Geldner, N. A mechanism for localized lignin deposition in the endodermis. *Cell* **153**, 402–412 (2013).
27. Asai, T. et al. MAP kinase signalling cascade in *Arabidopsis* innate immunity. *Nature* **415**, 977–983 (2002).
28. Smith, J. M. & Heese, A. Rapid bioassay to measure early reactive oxygen species production in *Arabidopsis* leave tissue in response to living *Pseudomonas syringae*. *Plant Methods* **10**, 6 (2014).
29. Suarez-Rodriguez, M. C. et al. MEKK1 is required for flg22-induced MPK4 activation in *Arabidopsis* plants. *Plant Physiol.* **143**, 661–669 (2007).
30. Liberman, L. M., Sparks, E. E., Moreno-Risueno, M. A., Petricka, J. J. & Benfey, P. N. MYB36 regulates the transition from proliferation to differentiation in the *Arabidopsis* root. *Proc. Natl Acad. Sci. USA* **112**, 12099–12104 (2015).
31. Zhou, F. et al. Co-incidence of damage and microbial patterns controls localized immune responses in roots. *Cell* **180**, 440–453.e18 (2020).
32. Emonet, A. et al. Spatially restricted immune responses are required for maintaining root meristematic activity upon detection of bacteria. *Curr. Biol.* **31**, 1012–1028.e7 (2021).
33. Roppolo, D. et al. Functional and evolutionary analysis of the Casparian strip membrane domain protein family. *Plant Physiol.* **165**, 1709–1722 (2014).
34. Roppolo, D. et al. A novel protein family mediates Casparian strip formation in the endodermis. *Nature* **473**, 380–383 (2011).

35. Li, B. et al. Phosphorylation of trihelix transcriptional repressor ASR3 by MAP KINASE4 negatively regulates *Arabidopsis* immunity. *Plant Cell* **27**, 839–856 (2015).
36. Barbosa, I. C. R. et al. Directed growth and fusion of membrane-wall microdomains requires CASP-mediated inhibition and displacement of secretory foci. *Nat. Commun.* **14**, 1626 (2023).
37. Rojas-Murcia, N. et al. High-order mutants reveal an essential requirement for peroxidases but not laccases in Casparian strip lignification. *Proc. Natl Acad. Sci. USA* **117**, 29166–29177 (2020).
38. Wang, P. et al. Surveillance of cell wall diffusion barrier integrity modulates water and solute transport in plants. *Sci. Rep.* **9**, 4227 (2019).
39. Popescu, S. C. et al. MAPK target networks in *Arabidopsis thaliana* revealed using functional protein microarrays. *Genes Dev.* **23**, 80–92 (2009).
40. Bi, G. et al. Receptor-like cytoplasmic kinases directly link diverse pattern recognition receptors to the activation of mitogen-activated protein kinase cascades in *Arabidopsis*. *Plant Cell* https://doi.org/10.1105/tpc.17.00981 (2018).
41. Li, X. et al. Flagellin induces innate immunity in non-host interactions that is suppressed by Pseudomonas syringae effectors. *Proc. Natl Acad. Sci. USA* **102**, 12990–12995 (2005).
42. Zhang, J. et al. A *Pseudomonas syringae* effector inactivates MAPKs to suppress PAMP-induced immunity in plants. *Cell Host Microbe* **1**, 175–185 (2007).
43. Zhang, Z. et al. Disruption of PAMP-induced MAP kinase cascade by a *Pseudomonas syringae* effector activates plant immunity mediated by the NB-LRR protein SUMM2. *Cell Host Microbe* **11**, 253–263 (2012).
44. Wang, H., Ngwenyama, N., Liu, Y., Walker, J. C. & Zhang, S. Stomatal development and patterning are regulated by environmentally responsive mitogen-activated protein kinases in *Arabidopsis*. *Plant Cell* **19**, 63–73 (2007).
45. Xu, J. et al. A chemical genetic approach demonstrates that MPK3/MPK6 activation and NADPH oxidase-mediated oxidative burst are two independent signaling events in plant immunity. *Plant J.* **77**, 222–234 (2014).
46. Su, J. et al. Regulation of stomatal immunity by interdependent functions of a pathogen-responsive MPK3/MPK6 cascade and abscisic acid. *Plant Cell* **29**, 526–542 (2017).
47. Ichimura, K. et al. Mitogen-activated protein kinase cascades in plants: a new nomenclature. *Trends Plant Sci.* **7**, 301–308 (2002).
48. Jiang, M. et al. Mitogen-activated protein kinase and substrate identification in plant growth and development. *Int. J. Mol. Sci.* **23**, 2744 (2022).
49. Andreasson, E. & Ellis, B. Convergence and specificity in the *Arabidopsis* MAPK nexus. *Trends Plant Sci.* **15**, 106–113 (2010).
50. Bi, G. & Zhou, J.-M. MAP kinase signaling pathways: a hub of plant–microbe interactions. *Cell Host Microbe* **21**, 270–273 (2017).
51. Xu, J. et al. Activation of MAPK kinase 9 induces ethylene and camalexin biosynthesis and enhances sensitivity to salt stress in *Arabidopsis*. *J. Biol. Chem.* **283**, 26996–27006 (2008).
52. Yoo, S.-D., Cho, Y.-H., Tena, G., Xiong, Y. & Sheen, J. Dual control of nuclear EIN3 by bifurcate MAPK cascades in C_2H_4 signalling. *Nature* **451**, 789–795 (2008).
53. Barberon, M. et al. Adaptation of root function by nutrient-induced plasticity of endodermal differentiation. *Cell* **164**, 447–459 (2016).
54. Tena, G., Boudsocq, M. & Sheen, J. Protein kinase signaling networks in plant innate immunity. *Curr. Opin. Plant Biol.* **14**, 519–529 (2011).
55. Mersmann, S., Bourdais, G., Rietz, S. & Robatzek, S. Ethylene signaling regulates accumulation of the FLS2 receptor and is required for the oxidative burst contributing to plant immunity. *Plant Physiol.* **154**, 391–400 (2010).
56. Tintor, N. et al. Layered pattern receptor signaling via ethylene and endogenous elicitor peptides during *Arabidopsis* immunity to bacterial infection. *Proc. Natl Acad. Sci. USA* **110**, 6211–6216 (2013).
57. Zhang, T. et al. Ethylene-induced stomatal closure is mediated via MKK1/3–MPK3/6 cascade to EIN2 and EIN3. *J. Integr. Plant Biol.* **63**, 1324–1340 (2021).
58. Rufián, J. S. et al. The bacterial effector HopZ1a acetylates MKK7 to suppress plant immunity. *New Phytol.* **231**, 1138–1156 (2021).
59. Baluška, F. & Mancuso, S. Deep evolutionary origins of neurobiology: turning the essence of 'neural' upside-down. *Commun. Integr. Biol.* **2**, 60–65 (2009).
60. Krysan, P. J. & Colcombet, J. Cellular complexity in MAPK signaling in plants: questions and emerging tools to answer them. *Front. Plant Sci.* **9**, 1674 (2018).
61. Bardwell, L., Zou, X., Nie, Q. & Komarova, N. L. Mathematical models of specificity in cell signaling. *Biophys. J.* **92**, 3425–3441 (2007).
62. Ma, Y. & Nicolet, J. Specificity models in MAPK cascade signalling. *FEBS Open Bio* https://doi.org/10.1002/2211-5463.13619 (2023).
63. Shigenaga, A. M. & Argueso, C. T. No hormone to rule them all: interactions of plant hormones during the responses of plants to pathogens. *Semin. Cell Dev. Biol.* **56**, 174–189 (2016).
64. Li, J.-R., Liu, C.-C., Sun, C.-H. & Chen, Y.-T. Plant stress RNA-seq nexus: a stress-specific transcriptome database in plant cells. *BMC Genomics* **19**, 966 (2018).
65. Kang, W.-H. et al. Transcriptome profiling of abiotic responses to heat, cold, salt, and osmotic stress of *Capsicum annuum* L. *Sci. Data* **7**, 17 (2020).
66. Cohen, S. P. & Leach, J. E. Abiotic and biotic stresses induce a core transcriptome response in rice. *Sci. Rep.* **9**, 6273 (2019).
67. Flagel, L. E. & Wendel, J. F. Gene duplication and evolutionary novelty in plants. *New Phytol.* **183**, 557–564 (2009).
68. Valmonte, G. R., Arthur, K., Higgins, C. M. & MacDiarmid, R. M. Calcium-dependent protein kinases in plants: evolution, expression and function. *Plant Cell Physiol.* **55**, 551–569 (2014).
69. Bardwell, L. Mechanisms of MAPK signalling specificity. *Biochem. Soc. Trans.* **34**, 837–841 (2006).
70. Raman, M., Chen, W. & Cobb, M. H. Differential regulation and properties of MAPKs. *Oncogene* **26**, 3100–3112 (2007).
71. Lee, J. S., Huh, K. W., Bhargava, A. & Ellis, B. E. Comprehensive analysis of protein–protein interactions between *Arabidopsis* MAPKs and MAPK kinases helps define potential MAPK signalling modules. *Plant Signal. Behav.* **3**, 1037–1041 (2008).
72. Feilner, T. et al. High throughput identification of potential *Arabidopsis* mitogen-activated protein kinases substrates. *Mol. Cell. Proteom.* **4**, 1558–1568 (2005).
73. Hoehenwarter, W. et al. Identification of novel in vivo MAP kinase substrates in *Arabidopsis thaliana* through use of tandem metal oxide affinity chromatography. *Mol. Cell. Proteom.* **12**, 369–380 (2013).
74. Yue, J. & López, J. M. Understanding MAPK signaling pathways in apoptosis. *Int. J. Mol. Sci.* **21**, 2346 (2020).
75. Danquah, A. et al. Identification and characterization of an ABA-activated MAP kinase cascade in *Arabidopsis thaliana*. *Plant J.* **82**, 232–244 (2015).
76. Sözen, C. et al. Wounding and insect feeding trigger two independent MAPK pathways with distinct regulation and kinetics. *Plant Cell* **32**, 1988–2003 (2020).
77. Menges, M. et al. Comprehensive gene expression atlas for the *Arabidopsis* MAP kinase signalling pathways. *New Phytol.* **179**, 643–662 (2008).
78. Schmid, M. et al. A gene expression map of *Arabidopsis thaliana* development. *Nat. Genet.* **37**, 501–506 (2005).

79. Chezem, W. R., Memon, A., Li, F.-S., Weng, J.-K. & Clay, N. K. SG2-type R2R3-MYB transcription factor MYB15 controls defense-induced lignification and basal immunity in *Arabidopsis*. *Plant Cell* **29**, 1907–1926 (2017).
80. Shukla, V. et al. Suberin plasticity to developmental and exogenous cues is regulated by a set of MYB transcription factors. *Proc. Natl Acad. Sci. USA* **118**, e2101730118 (2021).
81. Hoang, M. H. T. et al. Phosphorylation by AtMPK6 is required for the biological function of AtMYB41 in *Arabidopsis*. *Biochem. Biophys. Res. Commun.* **422**, 181–186 (2012).
82. Kim, S. H. et al. Phosphorylation of the transcriptional repressor MYB15 by mitogen-activated protein kinase 6 is required for freezing tolerance in *Arabidopsis*. *Nucleic Acids Res.* **45**, gkx417 (2017).
83. Rayapuram, N. et al. Quantitative phosphoproteomic analysis reveals shared and specific targets of *Arabidopsis* mitogen-activated protein kinases (MAPKs) MPK3, MPK4, and MPK6. *Mol. Cell. Proteom.* **17**, 61–80 (2018).
84. Lampard, G. R., Lukowitz, W., Ellis, B. E. & Bergmann, D. C. Novel and expanded roles for MAPK signaling in *Arabidopsis* stomatal cell fate revealed by cell type-specific manipulations. *Plant Cell* **21**, 3506–3517 (2009).
85. Wengier, D. L., Lampard, G. R. & Bergmann, D. C. Dissection of MAPK signaling specificity through protein engineering in a developmental context. *BMC Plant Biol.* **18**, 60 (2018).
86. Lampard, G. R., Wengier, D. L. & Bergmann, D. C. Manipulation of mitogen-activated protein kinase kinase signaling in the *Arabidopsis* stomatal lineage reveals motifs that contribute to protein localization and signaling specificity. *Plant Cell Online* **26**, 3358–3371 (2014).
87. Lu, X. et al. RGF1-RGI1, a peptide-receptor complex, regulates *Arabidopsis* root meristem development via a MAPK signaling cascade. *Mol. Plant* **13**, 1594–1607 (2020).
88. Ren, D., Yang, H. & Zhang, S. Cell death mediated by MAPK is associated with hydrogen peroxide production in *Arabidopsis*. *J. Biol. Chem.* **277**, 559–565 (2002).
89. Ichimura, K., Casais, C., Peck, S. C., Shinozaki, K. & Shirasu, K. MEKK1 is required for MPK4 activation and regulates tissue-specific and temperature-dependent cell death in *Arabidopsis*. *J. Biol. Chem.* **281**, 36969–36976 (2006).
90. Sun, T. et al. Antagonistic interactions between two MAP kinase cascades in plant development and immune signaling. *EMBO Rep.* **19**, e45324 (2018).
91. Kong, Q. et al. The MEKK1-MKK1/MKK2-MPK4 kinase cascade negatively regulates immunity mediated by a mitogen-activated protein kinase kinase kinase in *Arabidopsis*. *Plant Cell* **24**, 2225–2236 (2012).
92. Takagi, M. et al. Disruption of the MAMP-induced MEKK1-MKK1/MKK2-MPK4 pathway activates the TNL immune receptor SMN1/RPS6. *Plant Cell Physiol.* **60**, 778–787 (2018).
93. Takagi, M. et al. Simultaneous mutations in SMN1 and SUMM2 fully suppress the dwarf and autoimmune phenotypes of *Arabidopsis* mpk4 mutant. *Plant Signal. Behav.* **17**, 2046412 (2022).
94. Zhang, J. et al. MKK4/MKK5-MPK1/MPK2 cascade mediates SA-activated leaf senescence via phosphorylation of NPR1 in *Arabidopsis*. *Plant Mol. Biol.* **102**, 463–475 (2020).
95. Zhu, Q. et al. A MAPK cascade downstream of IDA–HAE/HSL2 ligand–receptor pair in lateral root emergence. *Nat. Plants* **5**, 414–423 (2019).
96. Goyal, R. K. et al. Analysis of MAPK and MAPKK gene families in wheat and related Triticeae species. *BMC Genomics* **19**, 178 (2018).
97. Romero-Hernandez, G. & Martinez, M. Opposite roles of MAPKKK17 and MAPKKK21 against *Tetranychus urticae* in *Arabidopsis*. *Front. Plant Sci.* **13**, 1038866 (2022).
98. Li, K. et al. AIK1, a mitogen-activated protein kinase, modulates abscisic acid responses through the MKK5-MPK6 kinase cascade. *Plant Physiol.* **173**, 1391–1408 (2016).
99. Zhao, C. et al. EDR1 physically interacts with MKK4/MKK5 and negatively regulates a MAP kinase cascade to modulate plant innate immunity. *PLoS Genet.* **10**, e1004389 (2014).
100. Gao, M. et al. MEKK1, MKK1/MKK2 and MPK4 function together in a mitogen-activated protein kinase cascade to regulate innate immunity in plants. *Cell Res.* **18**, 1190–1198 (2008).
101. Teige, M. et al. The MKK2 pathway mediates cold and salt stress signaling in *Arabidopsis*. *Mol. Cell* **15**, 141–152 (2004).
102. Dóczi, R. et al. The *Arabidopsis* mitogen-activated protein kinase kinase MKK3 is upstream of group C mitogen-activated protein kinases and participates in pathogen signaling. *Plant Cell* **19**, 3266–3279 (2007).
103. Siligato, R. et al. MultiSite gateway-compatible cell type-specific gene-inducible system for plants. *Plant Physiol.* **170**, 627–641 (2015).
104. Berriri, S. et al. Constitutively active mitogen-activated protein kinase versions reveal functions of *Arabidopsis* MPK4 in pathogen defense signaling. *Plant Cell* **24**, 4281–4293 (2012).
105. Clough, S. J. & Bent, A. F. Floral dip: a simplified method for *Agrobacterium*-mediated transformation of *Arabidopsis thaliana*. *Plant J.* **16**, 735–743 (1998).
106. Zhang, X., Henriques, R., Lin, S.-S., Niu, Q.-W. & Chua, N.-H. *Agrobacterium*-mediated transformation of *Arabidopsis thaliana* using the floral dip method. *Nat. Protoc.* **1**, 641–646 (2006).
107. Ursache, R., Fujita, S., Tendon, V. D. & Geldner, N. Combined fluorescent seed selection and multiplex CRISPR/Cas9 assembly for fast generation of multiple *Arabidopsis* mutants. *Plant Methods* **17**, 111 (2021).
108. Kurihara, D., Mizuta, Y., Sato, Y. & Higashiyama, T. ClearSee: a rapid optical clearing reagent for whole-plant fluorescence imaging. *Development* **142**, 4168–4179 (2015).
109. Ursache, R., Andersen, T. G., Marhavý, P. & Geldner, N. A protocol for combining fluorescent proteins with histological stains for diverse cell wall components. *Plant J.* **93**, 399–412 (2018).
110. Hepler, P. K., Fosket, D. E. & Newcomb, E. H. Lignification during secondary wall formation in *Coleus*: an electron microscopic study. *Am. J. Bot.* **57**, 85–96 (1970).
111. Kolbeck, A. et al. CASP microdomain formation requires cross cell wall stabilization of domains and non-cell autonomous action of LOTR1. *ELife* **11**, e69602 (2022).
112. Kremer, J. R., Mastronarde, D. N. & McIntosh, J. R. Computer visualization of three-dimensional image data using IMOD. *J. Struct. Biol.* **116**, 71–76 (1996).
113. Martin, M. Cutadapt removes adapter sequences from high-throughput sequencing reads. *EMBnet J.* **17**, 10–12 (2011).
114. Davis, M. P. A., van Dongen, S., Abreu-Goodger, C., Bartonicek, N. & Enright, A. J. Kraken: a set of tools for quality control and analysis of high-throughput sequence data. *Methods* **63**, 41–49 (2013).
115. Dobin, A. et al. STAR: ultrafast universal RNA-seq aligner. *Bioinformatics* **29**, 15–21 (2013).
116. Anders, S., Pyl, P. T. & Huber, W. HTSeq—a Python framework to work with high-throughput sequencing data. *Bioinformatics* **31**, 166–169 (2015).
117. Wang, L., Wang, S. & Li, W. RSeQC: quality control of RNA-seq experiments. *Bioinformatics* **28**, 2184–2185 (2012).
118. Robinson, M. D., McCarthy, D. J. & Smyth, G. K. edgeR: a Bioconductor package for differential expression analysis of digital gene expression data. *Bioinformatics* **26**, 139–140 (2010).
119. Ritchie, M. E. et al. limma powers differential expression analyses for RNA-sequencing and microarray studies. *Nucleic Acids Res.* **43**, e47 (2015).

120. Ursache, R. et al. GDSL-domain proteins have key roles in suberin polymerization and degradation. *Nat. Plants* **7**, 353–364 (2021).
121. Schneider, C. A., Rasband, W. S. & Eliceiri, K. W. NIH Image to ImageJ: 25 years of image analysis. *Nat. Methods* **9**, 671–675 (2012).

Acknowledgements

We thank the Cellular Imaging Facility (CIF), Genomic Technologies Facility (GTF) and Electron Microscopy Facility (EMF) of the University of Lausanne and N. Pullen for technical support; G. Ingram for critically reading the paper; S. Zhang and J. Colcombet for kindly sharing seed materials; and all Geldner lab members for sharing materials. Y.M. was supported by an EMBO non-stipendiary long-term fellowship (ALTF 711-2018), a FEBS Long-term Fellowship and by 20-MSCA-IF-2018 (grant number 846050). The work was supported by SNSF grant 310030 to N.G.

Author contributions

Y.M. and N.G. conceived, designed and coordinated the project. Y.M., I.F., J.N., J.P., J.B.D., D.D.B. and A.E. performed all experimental work and data analysis. S.F. and A.E. provided materials and were involved in the discussion of the work. Y.M. and N.G. wrote the paper with feedback from all co-authors.

Competing interests

The authors declare no competing interests.

Additional information

Extended data is available for this paper at https://doi.org/10.1038/s41477-024-01768-y.

Supplementary information The online version contains supplementary material available at https://doi.org/10.1038/s41477-024-01768-y.

Correspondence and requests for materials should be addressed to Yan Ma or Niko Geldner.

Peer review information *Nature Plants* thanks the anonymous reviewers for their contribution to the peer review of this work.

https://doi.org/10.1038/s41477-024-01768-y

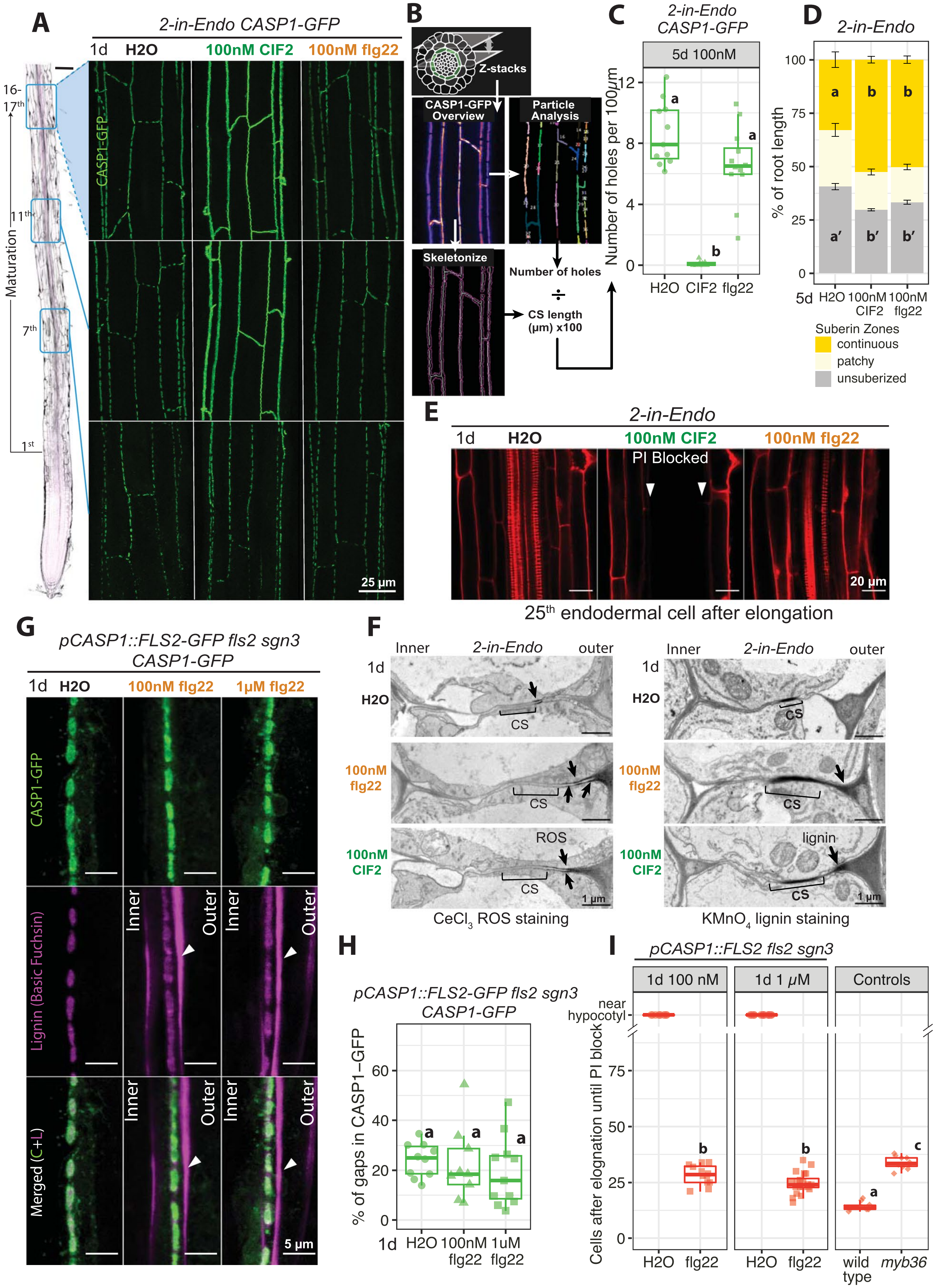

Extended Data Fig. 1 | See next page for caption.

Extended Data Fig. 1 | Endodermis-specific FLS2 induces ectopic lignin but cannot replace endogenous SGN3 for Casparian strip (CS) domain fusion. (**a**) CASP1-GFP overviews of *2-in-Endo* after 1d treatments of H_2O, 100 nM CIF2 or flg22 from initiation to maturation (7th, 11th, 16-17th endodermal cells after onset of elongation). (**b**) Schematics showing steps to quantify CS discontinuity in overviews to incorporate many more endodermal cells at once: 1. CASP1-GFP overviews: maximum projection of z-stacks capturing CS network in endodermal cell layer; 2. Particle Analysis (Fiji): count fragments and calculate corresponding number of holes; 3. Skeletonize (Fiji): convert area to lines and measure CS length in μm; 4. Calculate 'Number of holes per 100 µm' as in (C). (**c**) Quantification of CS discontinuity in *2-in-Endo* CASP1-GFP overviews at mature CS stage after constitutive (5d) treatments with H_2O, 100 nM CIF2 or 100 nM flg22 ($n \geq 8$). (**d**) Suberization quantification of *2-in-Endo* after constitutive (5d) treatments with H_2O, 100 nM CIF2 or flg22. Suberin was stained with Fluorol Yellow and quantified along the root axis divided by three zones: unsuberized (near the root-tip); patchy; and continuous (near hypocotyl). Data presented as percentage of total root length (Mean ± SE; $n = 10$). Zones with the same letter are not significantly different among treatments ($p < 0.05$, one-way ANOVA and Tukey test). (**e**) Diffusion barrier of *2-in-Endo* visualized by Propidium Iodide (PI, red) penetration at 25th endodermal cell after onset of elongation. Arrowheads mark PI signal exclusion from the inner side of an endodermal cell (PI block). (**f**) Transmission Electron Microscopy (TEM) showing *in situ* H_2O_2 (ROS) detection with $CeCl_3$ (left) and lignin detection with $KMnO_4$ (right) at the CS of *2-in-Endo* after 1d H_2O, 100 nM CIF2 or flg22 treatments. Micrographs obtained from sections ~1.5 mm away from the root tip. Brackets indicate CS: uniformly light grey cell wall areas with membrane attachment (left) and dense black staining (right). Arrowheads indicate ectopic accumulations of ROS (left) and lignin (right). (**g**) CS & CASP1 domain fusion phenotypes of *pCASP1::FLS2-GFP fls2 sgn3 CASP1-GFP* after 1d treatment with H_2O, 100 nM flg22 or 1 µM flg22. Endodermal cell surface views at mature CS stage (16-17th cell) show CASP1-GFP (green), lignin stained with Basic Fuchsin (magenta) and overlaps of the two channels (Merged). Arrowheads highlight ectopic lignin. 'outer', cortex-facing, 'inner', stele-facing endodermal surface. (**h**) Quantifications for (G) showing the percentage of gaps in CASP1-GFP *pCASP1::FLS2-GFP fls2 sgn3* after 1d treatments ($n \geq 9$). (**i**) PI penetration assay quantifies the CS barrier function of *pCASP1::FLS2-GFP fls2 sgn3* with 1d treatments of H_2O and flg22 at 100 nM and 1 µM concentrations compared to controls. Roots with no barrier show PI penetration near root-hypocotyl junction, shown in the 'near hypocotyl' category and are excluded from numerical statistical test ($n \geq 10$). For (C)(H)(I), groups with the same letter are not significantly different ($P < 0.05$, one-way ANOVA and Tukey test). Unbalanced Tukey test used for unequal replication.

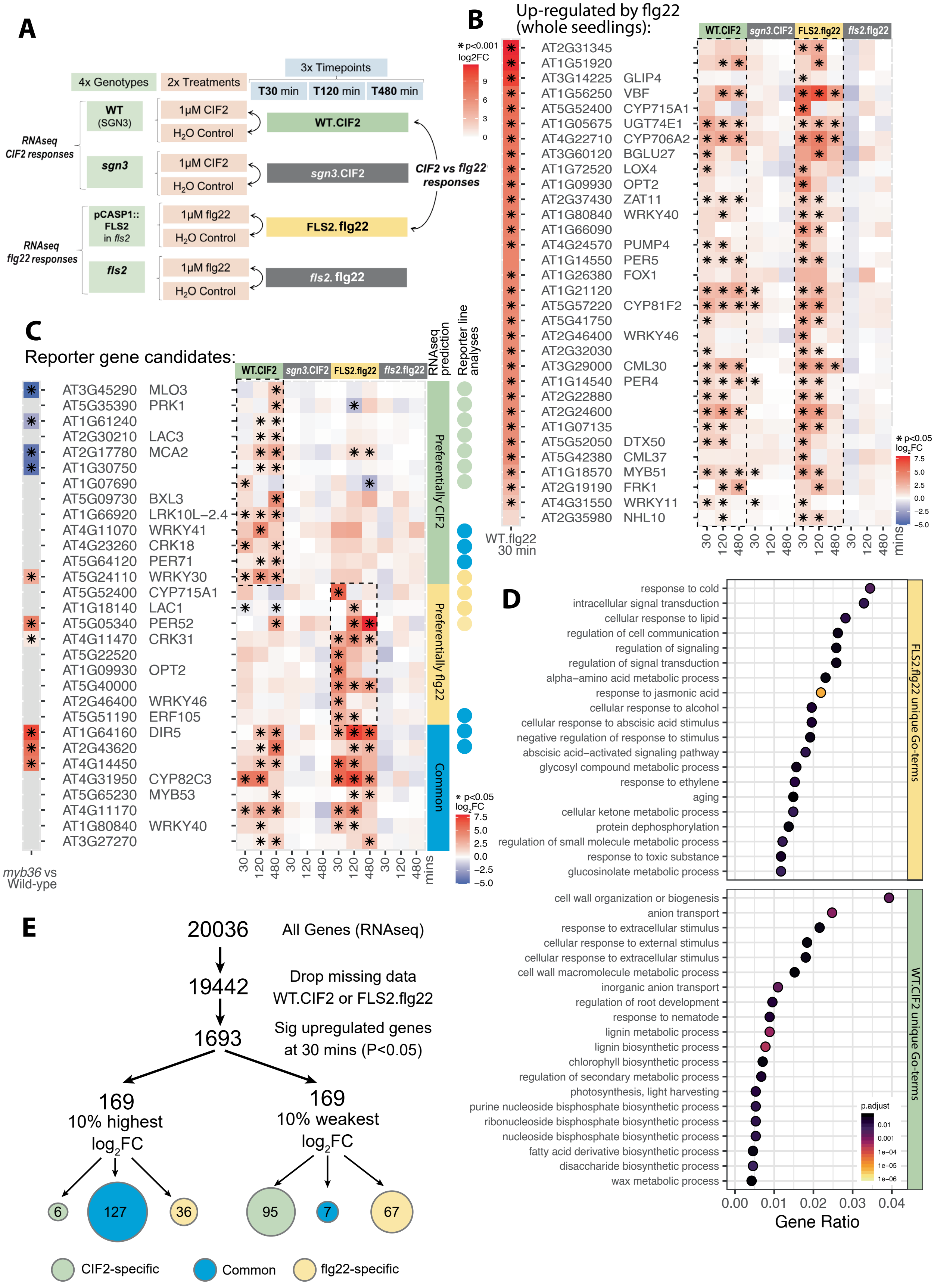

Extended Data Fig. 2 | See next page for caption.

Extended Data Fig. 2 | Endodermis-expressed FLS2 and SGN3 activate both common and pathway-specific transcriptional responses. (**a**) Experimental setups for RNAseq analysis comparing CIF2 and flg22 responses in root endodermis. Transcriptional data for CIF2 responses are from Fujita et al.[20]. WT.CIF2, *sgn3*.CIF2: wild-type with functional SGN3 and *sgn3* treated with 1 µM CIF2 vs H_2O control. FLS2.flg22, *fls2*.flg22: pCASP1::FLS2-GFP *fls2* and *fls2* treated with 1 µM flg22 vs H_2O control. Fold change ($\log_2$FC) were calculated by comparing peptide (1 µM flg22 or 1 µM CIF2) to H_2O treatment at each time point (30, 120, 480 mins). (**b**) Heatmaps of genes regulated by FLS2 in whole seedlings – significantly upregulated genes in flg22-treated wild-type (left) (*, $P < 0.001$)[35] – are also strongly induced by CIF2 (WT.CIF2) and flg22 (FLS2.flg22) in the endodermis (right) (*$P < 0.05$). Colour code: fold change degree ($\log_2$FC). (**c**) Heatmaps of fold change for reporter genes. Candidates are predicted to be preferentially CIF2 (green) or flg22 (yellow) responsive, or equally responsive (blue) in the endodermis (*$P < 0.05$). Reporter line analyses for selected genes are shown on the right (circles), with colour indicating observed pathway specificity (details see Supplementary Table 1). Corresponding heatmap of fold-change in *myb36* compared to Wild-type (*$P < 0.001$, NA in grey)[30] shown on the left. Colour code: fold change degree ($\log_2$FC). (**d**) Gene ontology (GO) enrichment analysis showing enriched GO-terms unique to FLS2 and SGN3 pathways upon stimulation in the endodermis. Colour: GO-enrichment significance. Dot size: gene ratio (the gene counts in a GO category differentially regulated by a pathway divided by the total number of genes in that GO category). (**e**) Workflow to determine the pathway specificity of top 10% most responsive genes and least responsive ($P < 0.05$, ranked by Log_2FC) at 30 min. Genes that are significantly upregulated by one pathway but not the other are considered specific, genes that are significantly upregulated by both are considered common (Cut-off: $\text{Log}_2\text{FC} > 1$ and $P < 0.05$).

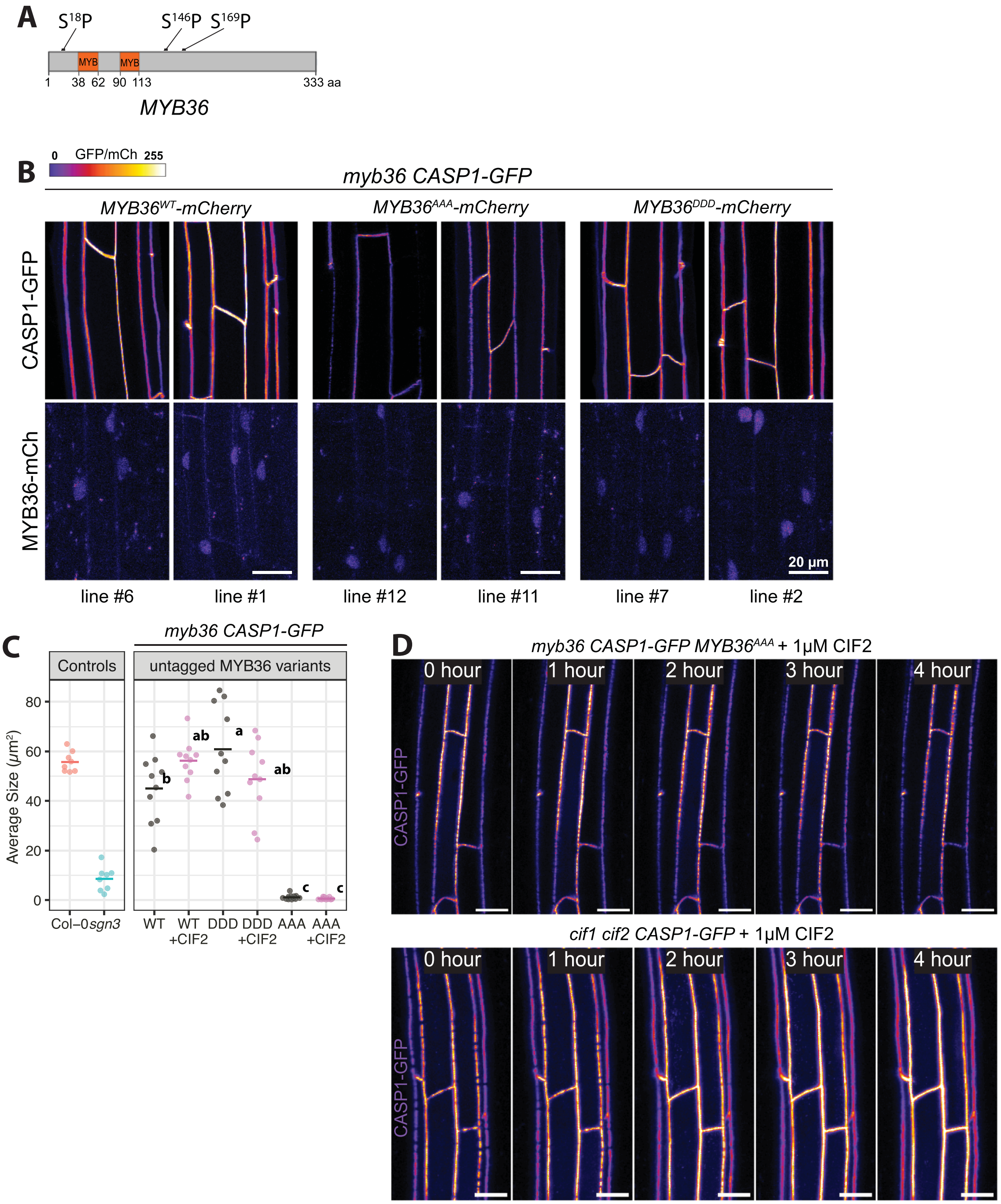

Extended Data Fig. 3 | Predicted phospho-sites of MYB36 are crucial for SGN-dependent CASP and CS domain fusion. (**a**) *MYB36* protein diagram, with locations of three putative MPK phosphorylation sites (Serine Proline - SP) and two MYB-type HTH DNA binding domains (MYB). (**b**) CASP1-GFP phenotypes and MYB36 accumulations in *myb36 CASP1-GFP* transformed with *MYB36^{WT}-mCherry*, *MYB36^{AAA}-mCherry*, *MYB36^{DDD}-mCherry*. CASP1-GFP overviews (upper-panels) at 16-17th cell and MYB36-mCherry nuclei signals (lower-panels) from the same lines at 7-8th cells are shown for each genotype. GFP and mCherry in gradient intensity. (**c**) Quantification of CASP1 domain property: Average size of CASP1-GFP fragments in surface views, same data as Fig. 3c. *myb36 CASP1-GFP* transformed with untagged MYB36^{WT}, MYB36^{AAA}, MYB36^{DDD} (WT, AAA, DDD) are treated with 1d H2O (grey) and 1 µM CIF2 (pink) ($n \geq 10$). (**d**) CASP1-GFP time lapse images of *myb36 CASP1-GFP untagged MYB36^{AAA}* (top) and *cif1 cfi2 CASP1-GFP* (bottom) treated with 1 µM CIF2 from 0-4 hours. Maximum projections of roots at mature CS (16-17th cell) are shown. Scale bars = 20 µm.

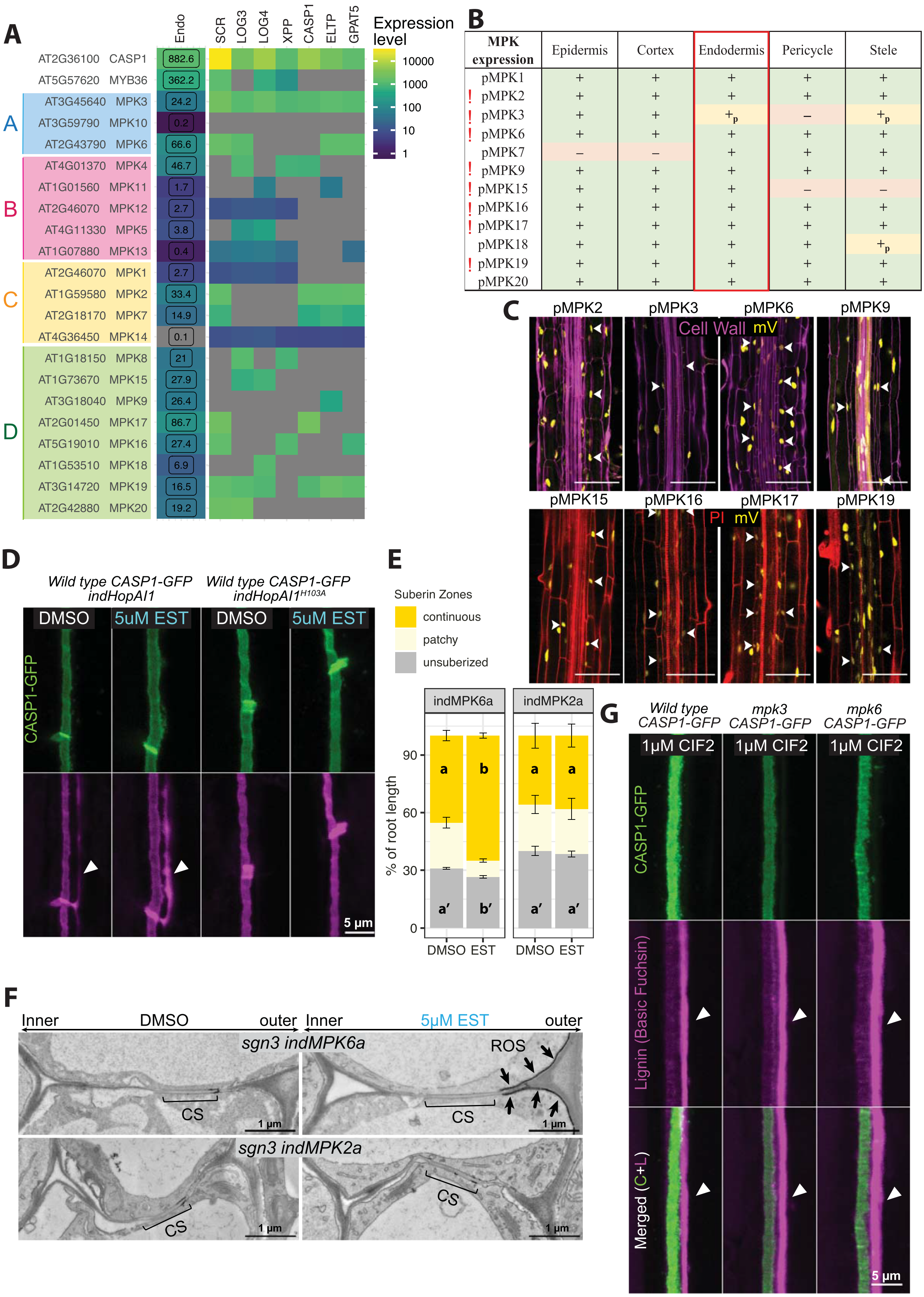

MPK expression	Epidermis	Cortex	Endodermis	Pericycle	Stele
pMPK1	+	+	+	+	+
! pMPK2	+	+	+	+	+
! pMPK3	+	+	$+_p$	–	$+_p$
! pMPK6	+	+	+	+	+
pMPK7	–	–	+	+	+
! pMPK9	+	+	+	+	+
! pMPK15	+	+	+	–	–
! pMPK16	+	+	+	+	+
! pMPK17	+	+	+	+	+
pMPK18	+	+	+	+	$+_p$
! pMPK19	+	+	+	+	+
pMPK20	+	+	+	+	+

Extended Data Fig. 4 | See next page for caption.

Extended Data Fig. 4 | Multiple MPKs contribute to CS integrity downstream of the SGN3 pathway. **(a)** MPK expression analysis in the endodermis. MPKs 1-20 from *Arabidopsis thaliana* are classified into 4 phylogenetic groups using full length sequences[47]. Endodermis-enriched RNA-seq data[30] (Endo) and Translating Ribosomal Affinity Purification (TRAP) analysis (Andersen & Vermeer, *personal communication*) that detect mRNA transcripts in distinct compartments of endodermis and xylem poles using different promoters: SCR (Meristematic endodermis); LOG3 (Xylem pole protoxylem); LOG4 (Xylem pole endodermis); XPP (Xylem pole); CASP1 (Early unsuberized endodermis); ELTP or LTPG15 (The entire differentiated endodermis); GPAT5 (Suberized endodermis). CASP1 and MYB36 are used as references. **(b)** MPKs with endodermal expression around CS initiation (7-8th cell). Analyses based on individual *pMPK::NLS-3xmVenus* lines (1 to 20) in wild-type. See Supplementary Table 3 for full atlas analysis. Expression in all cells (green +), expression in some but not all cells (yellow $+_p$), no expression in all cells (red −). '!' marks the selected MPKs for further analyses. (**c**) Examples of *pMPK::NLS-3xmVenus* reporter with endodermal signals during CS development. White arrows indicate endodermal nuclei. Cell walls are stained with Calcofluor white (magenta – upper) or with PI (red – lower). Scale bars = 100 µm. (**d**) CASP1-GFP phenotype with endodermal suppression of multiple MPK activities by inducing HopAI1 *vs*. inactive HopAI^{H103A} in wild-type at 16-17th cell. (**e**) Suberization quantification with or without MPK6a or MPK2a induction in *sgn3 CASP1-GFP*. Suberin stained with Fluorol Yellow and quantified along the root axis divided by three zones: unsuberized; patchy; and continuous. Data presented as percentage of total root length (Mean ± SE; n ≥ 10). Zones with the same letter are not significantly different ($p < 0.001$, Student's t-test). (**f**) TEM showing *in situ* H_2O_2 (ROS) detection with $CeCl_3$ at the CS of *2-in-Endo* after 5d DMSO control or EST induction of MPK6a and MPK2a in *sgn3 CASP1-GFP*. Micrographs obtained from sections ~3 mm from the root tip. Brackets indicate CS: uniformly light grey cell wall areas with membrane attachment. Arrowheads indicate accumulations of ROS at endodermal cell corners. (**g**) CS lignin & CASP1 phenotypes of *mpk3* and *mpk6* compared to wild-type, after 1d treatment of 1 µM CIF2. Surface views at 16-17th cell show CASP1-GFP (green), Lignin (magenta) and channel overlaps (Merged). Arrowheads highlight ectopic lignin on the cortex-facing side.

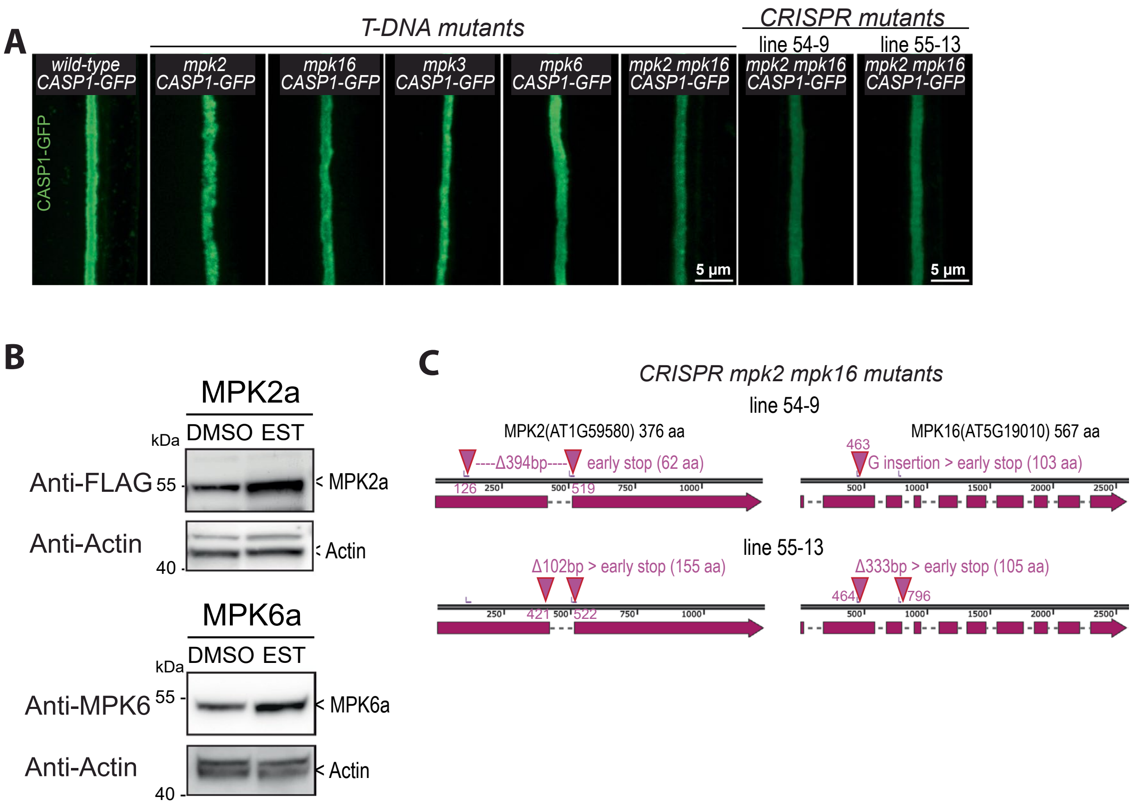

Extended Data Fig. 5 | Multiple MPKs contribute to CS integrity downstream of the SGN3 pathway (continued). (**a**) CASP1 phenotypes of T-DNA mutants *mpk2, mpk16, mpk3, mpk6, mpk2 mpk16* and two independent lines of *mpk2 mpk16* CRIPSR mutants. CASP1-GFP surface views at 16-17th cell are shown. (**b**) Immunoblot (IB) against anti-FLAG shows accumulations of the C-terminally 3xFLAG tagged MPK2a in *sgn3 CASP1-GFP* background. IB against MPK6 shows accumulations of MPK6a in *sgn3 CASP1-GFP* background. T3 seedling roots grown on DMSO or 5 µM EST were harvested. Loading controls: IBs with anti-Actin antibody or Ponceau S staining. See Supplementary Fig. 7 for uncropped original blots. This experiment was repeated three times. (**c**) Allelic information of two independent *mpk2 mpk16* CRIPSR mutant lines. Pink arrowheads indicate positions for homozygous deletions or insertion. Amino acid numbers in brackets indicate the size of protein fragment due to early stop codon. gRNAs used to target MPK2 and MPK16 see Supplementary Table 4.

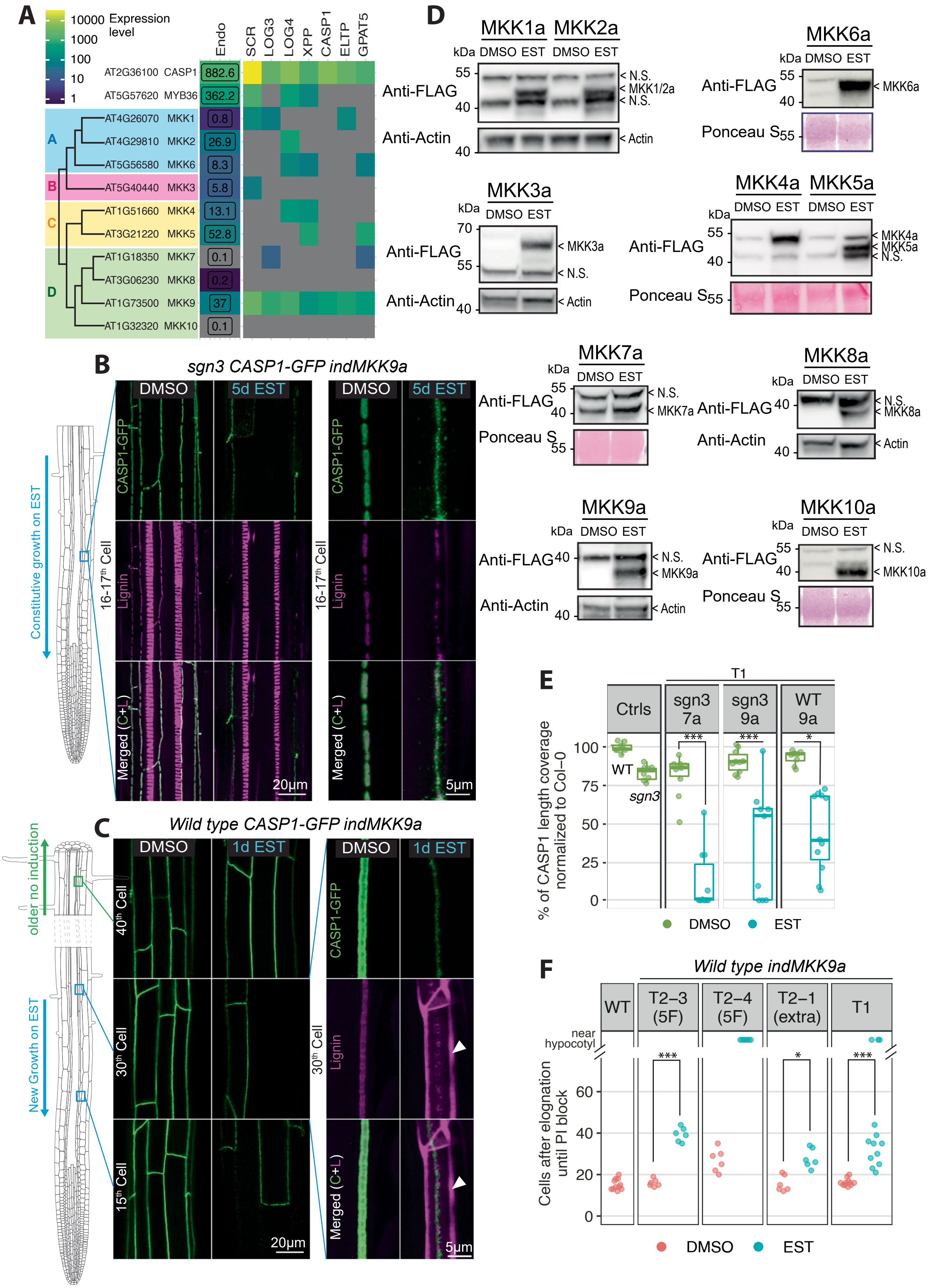

Extended Data Fig. 6 | See next page for caption.

Extended Data Fig. 6 | Activation of individual MKKs in the endodermis produces distinct outputs. (**a**) MKK expression analysis in the endodermis. MKKs 1-10 from *Arabidopsis thaliana* are classified into 4 phylogenetic groups using full length sequence[47]. Endodermis-enriched RNA-seq data[30] (Endo) and TRAP analysis (Andersen & Vermeer, *personal communication*) that detect mRNA transcripts in distinct compartments of endodermis and xylem poles using different promoters: SCR (Meristematic endodermis); LOG3 (Xylem pole protoxylem); LOG4 (Xylem pole endodermis); XPP (Xylem pole); CASP1 (Early unsuberized endodermis); ELTP or LTPG15 (The entire differentiated endodermis); GPAT5 (Suberized endodermis). (**b**) CASP1 & lignin phenotypes upon EST induction of MKK9a in *sgn3 CASP1-GFP* at 16-17th cell. Left panels show overviews and right panels show surface views with partial suppression for CASP1-GFP (green), Lignin (magenta) and channel overlaps (Merged). (**c**) CASP1 phenotypes after one-day EST induction of MKK9a in *wild-type CASP1-GFP* at new growth (15th and 30th cell -EST induction), and older growth (40th cell - no induction). Right panels show zoomed surface views at 30th cell for CASP1-GFP (green), lignin (magenta) and channel overlaps (Merged). Arrowheads highlight ectopic lignin on the cortex-facing side. (**d**) Immunoblots (IB) against anti-FLAG showing accumulations of the C-terminally 3xFLAG tagged indMKK1-10a in *sgn3 CASP1-GFP* background upon EST induction. T3 seedlings roots grown on DMSO or 5 μM EST were harvested. N.S., non-specific bands. Loading controls: IBs with anti-Actin antibody or Ponceau S staining. See Supplementary Fig. 7 for uncropped original blots. This experiment was repeated two to three times. (**e**) Quantification of CS coverage upon induction of MKK7a and MKK9a in *sgn3 CASP1-GFP*, MKK9a in *WT CASP1-GFP* (T1 roots, $n \geq 8$). At mature CS stage, total CASP1 length of each overview image measured normalized to the average CASP1-GFP length in wild-type to calculate percentage of CS coverage for each data point. (**f**) PI penetration assay upon endodermal induction of MKK9a in *WT CASP1-GFP* ($n \geq 10$). Data from three independent T2 lines and independent T1 seedlings are included (T2-3 and T2-4 data are shown in Fig. 5f). For (E)(F), Welch's T-test compares DMSO with EST for each genotype, p-values were adjusted for multiple comparisons by Bonferroni correction (***$p < 0.001$, **$p < 0.01$, *$p < 0.05$). For EST induction, all seedlings were grown for 5d on 5 μM EST or DMSO.

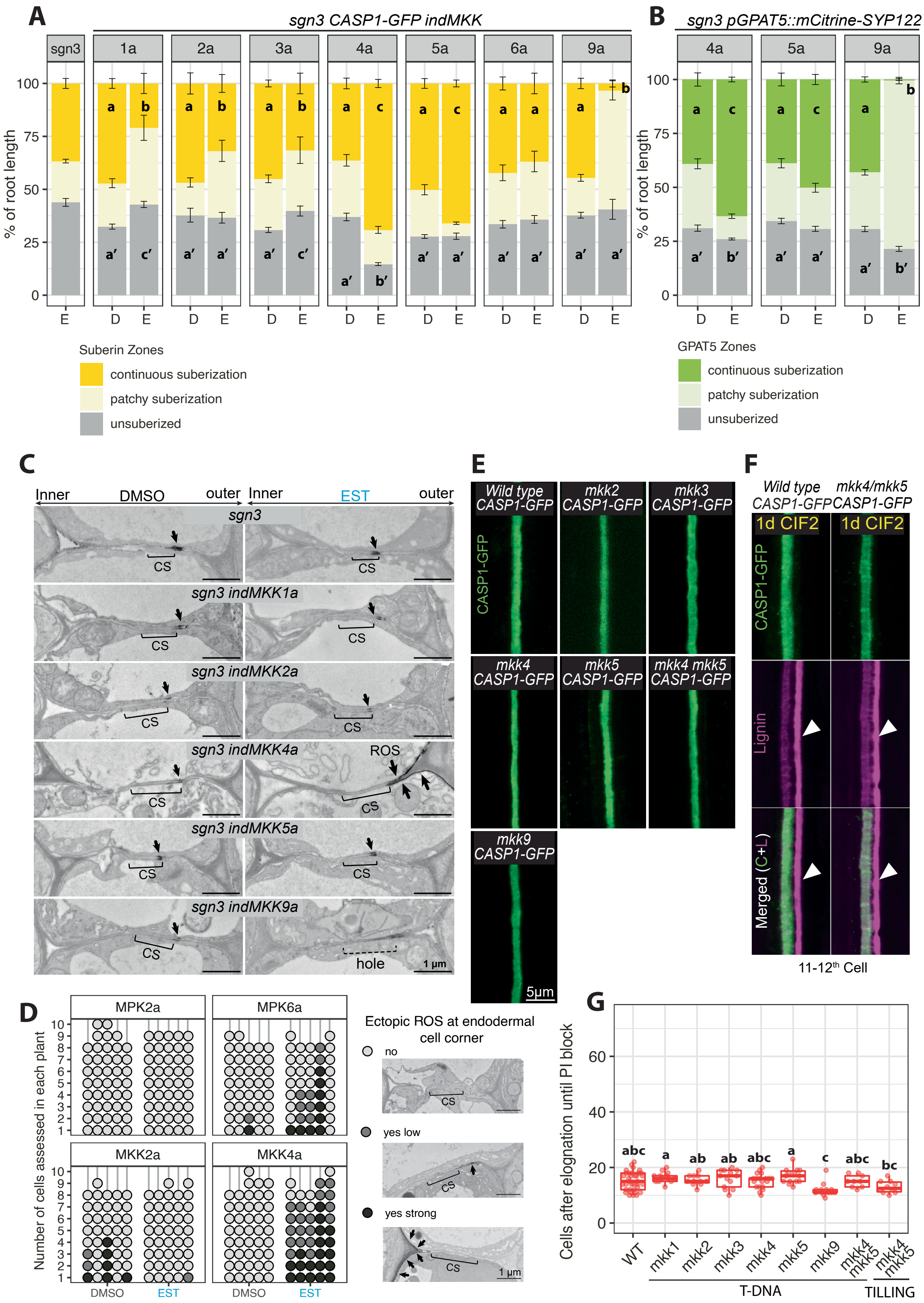

Extended Data Fig. 7 | See next page for caption.

Extended Data Fig. 7 | Activation of individual MKKs in the endodermis produces distinct outputs (continued). (**a**) Suberization quantification upon induction of MKK1/2/3/4/5/6/9a in *sgn3 CASP1-GFP*. Suberin stained with Fluorol Yellow and quantified along the root axis divided by three zones: unsuberized; patchy; and continuous. Data presented as percentage of total root length (Mean ± SE; $n \geq 10$). (**b**) Suberin synthesis quantification upon induction of MKK4a, MKK5a and MKK9a in *sgn3 pGPAT5::mCitrine-SYP122* (SYP122 is a membrane marker). Suberin synthesis is marked by *GPAT5* transcription. Data presented as percentage of total root length (Mean ± SE; $n \geq 10$). Zones in each genotype with the same letter are not significantly different upon treatment ($p < 0.05$, Student's t-test for equal replicates, Welch's t-test for unequal replicates). Zones with c/c' are increased compared to a/a', b/b' decreased compared to a/a'. (**c**) TEM showing *in situ* H_2O_2 (ROS) detection with $CeCl_3$ at the CS of *2-in-Endo* after 5d DMSO or EST induction of MKK1/2/3/4/5/9a in *sgn3 CASP1-GFP*. Micrographs obtained from sections ~1.5-2 mm from the root tip. Brackets indicate CS: uniformly light grey cell wall areas with membrane attachment. Dashed bracket indicates the absence of an CS. Arrowheads indicate accumulations of ROS. (**d**) TEM quantification of ectopic ROS at endodermal cell corner after 5d DMSO or EST induction of induction MPK2a, MPK6a, MKK2a and MKK4a in *sgn3 CASP1-GFP*. All samples were collected, prepared, and imaged from a single experiment. Each horizontal line represents a single root. Each dot represents an endodermal cell. Different coloured dots illustrate the categorization of ectopic ROS phenotypes (no, yes low, yes strong) which representative images on the right. (**e**) CASP1 phenotypes of *mkk2, mkk3, mkk4, mkk5, mkk9, mkk4 mkk5* at 16-17th cell. (**f**) CASP1 & lignin phenotypes of one-day 1 µM CIF2 treated wild-type and *mkk4 mkk5 CASP1-GFP* at 11-12th Cell. Arrowheads highlight ectopic lignin on cortex-facing side. (**g**) PI penetration assay quantifies the CS barrier function of T-DNA mutants *mkk1, mkk2, mkk3, mkk4, mkk5, mkk9, mkk4 mkk5* and *mkk4 mkk5* (TILLING) ($n \geq 10$). Groups with the same letter are not significantly different ($P < 0.05$, one-way ANOVA and Tukey HSD). For EST induction, all seedlings were grown for 5 d on 5 µM EST or DMSO control before analysis unless indicated otherwise.

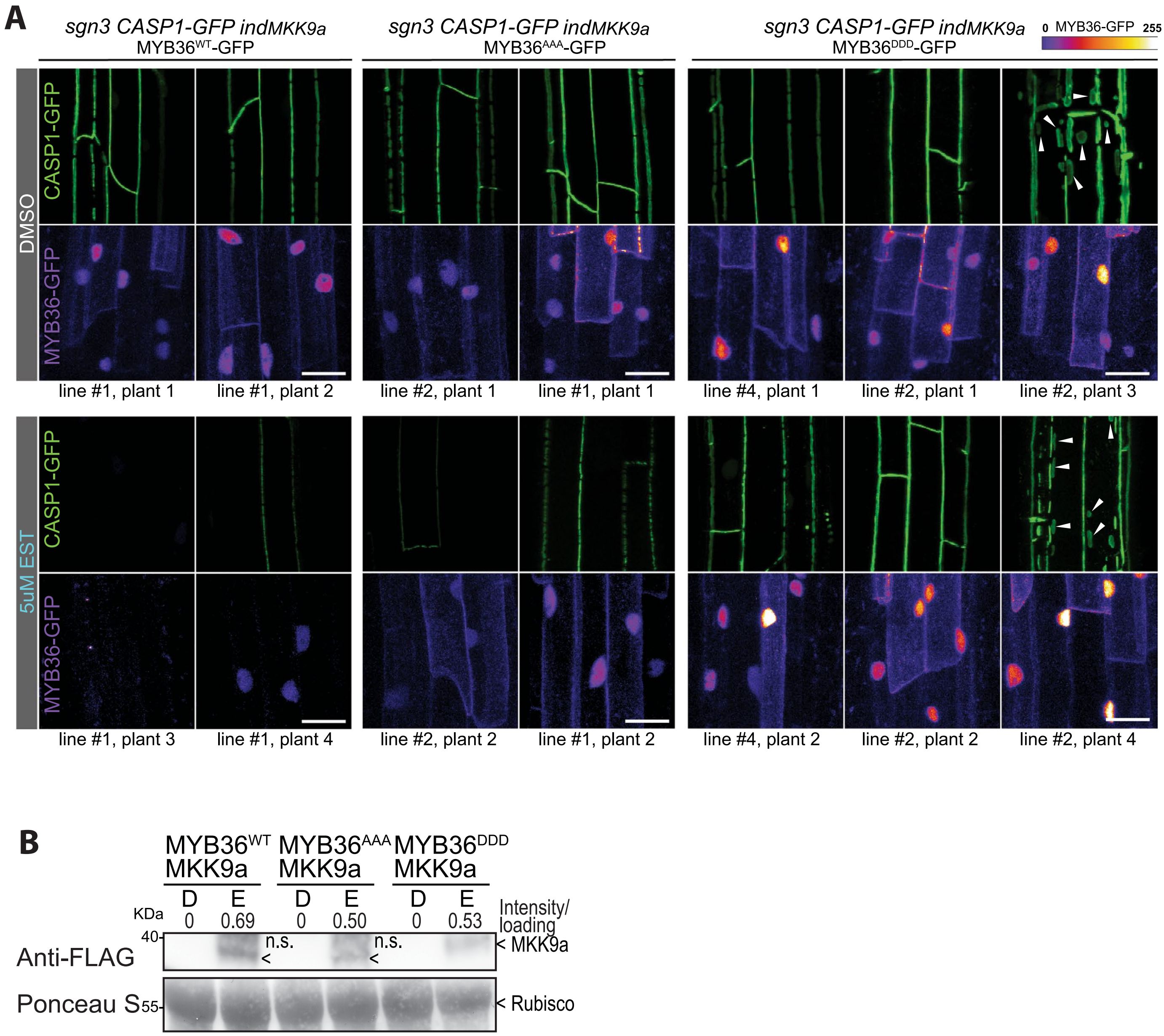

Extended Data Fig. 8 | Constitutively active MKK9 inhibits CS formation via suppressing MYB36. (**a**) CASP1-GFP and corresponding MYB36 accumulations in *sgn3 CASP1-GFP indMKK9a* transformed with MYB36^{WT}-GFP, MYB36^{AAA}-GFP, MYB36^{DDD}-GFP with or without EST induction. CASP1-GFP overviews from different plant lines at mature CS stage (16-17th cell) are shown in upper panels. Nuclei signals of MYB36-GFP from the same lines are taken around the onset of CASP1-GFP (7-8th cells) and shown in corresponding panels below. GFP signals are shown in gradient intensity. Scale bars = 20 µm. (**b**) Immunoblots (IB) against anti-FLAG show accumulations of the C-terminally 3xFLAG tagged indMKK9a in *sgn3 CASP1-GFP* (T3 homozygous for MKK9a) transformed with MYB36^{WT}-GFP, MYB36^{AAA}-GFP, MYB36^{DDD}-GFP with and without EST induction. Seedling roots of the same T2 lines used in Fig. 6a–d were grown on DMSO or 5 µM EST. Loading controls: IBs with anti-Actin antibody. Numbers above each lane show the FLAG (MKK9a) intensity normalized to corresponding Actin loading control. '>' indicate MKK9a, 'n.s.' indicate non-specific bands. See Supplementary Fig. 7 for uncropped original blots. Due to limited seed material, this experiment could only be performed once.

nature portfolio

Corresponding author(s): Yan Ma, Niko Geldner

Last updated by author(s): 13/07/24

Reporting Summary

Nature Portfolio wishes to improve the reproducibility of the work that we publish. This form provides structure for consistency and transparency in reporting. For further information on Nature Portfolio policies, see our Editorial Policies and the Editorial Policy Checklist.

Statistics

For all statistical analyses, confirm that the following items are present in the figure legend, table legend, main text, or Methods section.

n/a	Confirmed	
☐	☒	The exact sample size (*n*) for each experimental group/condition, given as a discrete number and unit of measurement
☐	☒	A statement on whether measurements were taken from distinct samples or whether the same sample was measured repeatedly
☐	☒	The statistical test(s) used AND whether they are one- or two-sided *Only common tests should be described solely by name; describe more complex techniques in the Methods section.*
☒	☐	A description of all covariates tested
☐	☒	A description of any assumptions or corrections, such as tests of normality and adjustment for multiple comparisons
☐	☒	A full description of the statistical parameters including central tendency (e.g. means) or other basic estimates (e.g. regression coefficient) AND variation (e.g. standard deviation) or associated estimates of uncertainty (e.g. confidence intervals)
☐	☒	For null hypothesis testing, the test statistic (e.g. *F*, *t*, *r*) with confidence intervals, effect sizes, degrees of freedom and *P* value noted *Give P values as exact values whenever suitable.*
☒	☐	For Bayesian analysis, information on the choice of priors and Markov chain Monte Carlo settings
☒	☐	For hierarchical and complex designs, identification of the appropriate level for tests and full reporting of outcomes
☒	☐	Estimates of effect sizes (e.g. Cohen's *d*, Pearson's *r*), indicating how they were calculated

Our web collection on statistics for biologists contains articles on many of the points above.

Software and code

Policy information about availability of computer code

Data collection	No specialist Softwares were used for data collection.
Data analysis	Open softwares used for data processing and analyses have been listed at the end of the Resource Table (Table S5). Fiji (ImageJ2) Version:2.9.0/1.53t, R 4.0.4; IMOD 4.11(3dmod). Detailed packages and versions used for RNAseq analysis are described in detail in the Method section.

For manuscripts utilizing custom algorithms or software that are central to the research but not yet described in published literature, software must be made available to editors and reviewers. We strongly encourage code deposition in a community repository (e.g. GitHub). See the Nature Portfolio guidelines for submitting code & software for further information.

Data

Policy information about availability of data

All manuscripts must include a data availability statement. This statement should provide the following information, where applicable:

- Accession codes, unique identifiers, or web links for publicly available datasets
- A description of any restrictions on data availability
- For clinical datasets or third party data, please ensure that the statement adheres to our policy

Materials Availability: Plasmids and transgenic plant seeds generated in this study will be made available on request, but we may require a payment and/or a completed Materials Transfer Agreement if there is potential for commercial application.

Data and Code Availability: The full RNA-seq dataset is deposited in NCBI GEO accession number GSE270950. All this data is publicly available upon publication by default. This study does not generate new code. R scripts used to generate graphs or Fiji Macros used for image processing and quantifications will be made available on request.

Research involving human participants, their data, or biological material

Policy information about studies with human participants or human data. See also policy information about sex, gender (identity/presentation), and sexual orientation and race, ethnicity and racism.

Reporting on sex and gender	N/A
Reporting on race, ethnicity, or other socially relevant groupings	N/A
Population characteristics	N/A
Recruitment	N/A
Ethics oversight	N/A

Note that full information on the approval of the study protocol must also be provided in the manuscript.

Field-specific reporting

Please select the one below that is the best fit for your research. If you are not sure, read the appropriate sections before making your selection.

☒ Life sciences ☐ Behavioural & social sciences ☐ Ecological, evolutionary & environmental sciences

For a reference copy of the document with all sections, see nature.com/documents/nr-reporting-summary-flat.pdf

Life sciences study design

All studies must disclose on these points even when the disclosure is negative.

Sample size	Sample size for replication was determined based on practicality and reliability of the biological assays conducted. We are guided by assays established in previous publications, e.g., PI penetration assay, suberin coverage quantification, Number of holes in CASP1 quantification, and TEM ROS quantification. Details in Figure Legend and Method. Citations: Doblas, V. G. et al. Root diffusion barrier control by a vasculature-derived peptide binding to the SGN3 receptor. Science 355, 280–284 (2017). Fujita, S. et al. SCHENGEN receptor module drives localized ROS production and lignification in plant roots. Embo J e103894 (2020) doi:10.15252/embj.2019103894; Emonet, A. et al. Spatially Restricted Immune Responses Are Required for Maintaining Root Meristematic Activity upon Detection of Bacteria. Curr. Biology 31, 1012-1028.e7 (2021).
Data exclusions	No data were specifically excluded from the analysis.
Replication	For replication of microscopy imaging data, attempts at replication were successful and Figure panels display representative images chosen from replication. For quantification and biological assays in transgenic plant lines, care was taken to include individual plants from the same plant line as well as an independent plant line. For phenotypic quantifications were carried out in at least two independent biological replicates with consistent results. Controls combine data from different biological replicates where relevant. For western blots, at least two attempts at replication were successful.
Randomization	For three independent biological replicates of RNAseq samples (non-random effects), data was corrected for the experimental batch effect using removeBatchEffect function (limma). For other experiments, groups were decided by genotypes, so no random allocation is required.
Blinding	Blinding of genetic background and/or treatments when conducting biological experiments were adopted where appropriate (Figure 1,3, 4B, 6A-D). In these cases, the investigator only knew the genotypes or treatments by code when conducting the experiments. In other cases, blinding was difficult due to obvious phenotypic differences between treatments and genotypes.

Reporting for specific materials, systems and methods

We require information from authors about some types of materials, experimental systems and methods used in many studies. Here, indicate whether each material, system or method listed is relevant to your study. If you are not sure if a list item applies to your research, read the appropriate section before selecting a response.

Materials & experimental systems

n/a	Involved in the study	
☐	☒	Antibodies
☒	☐	Eukaryotic cell lines
☒	☐	Palaeontology and archaeology
☒	☐	Animals and other organisms
☒	☐	Clinical data
☒	☐	Dual use research of concern
☐	☒	Plants

Methods

n/a	Involved in the study	
☒	☐	ChIP-seq
☒	☐	Flow cytometry
☒	☐	MRI-based neuroimaging

Antibodies

Antibodies used	Phospho-p44/42 MAPK (Erk1/2) (Thr202/Tyr204) (D13.14.4E) XP Rabbit mAb (Cell Signaling Technologies 4370; anti-AtMPK6 rabbit Sigma A7104; Monoclonal anti-FLAG M2 Peroxidase (HRP) mouse Sigma A8592; Monoclonal anti-Actin clone 16-B6 (Mab13a) mouse Sigma A0605; Secondary anti rabbit HRP Agrisera; Secondary anti mouse IgG HRP conjugate Promega W402B
Validation	https://www.cellsignal.com/products/primary-antibodies/phospho-p44-42-mapk-erk1-2-thr202-tyr204-d13-14-4e-xp-rabbit-mab/4370 https://www.sigmaaldrich.com/AT/en/product/sigma/a7104 https://www.sigmaaldrich.com/AT/en/product/sigma/a8592 https://www.sigmaaldrich.com/AT/en/product/sigma/a0605

Dual use research of concern

Policy information about dual use research of concern

Hazards

Could the accidental, deliberate or reckless misuse of agents or technologies generated in the work, or the application of information presented in the manuscript, pose a threat to:

No	Yes	
☐	☐	Public health
☐	☐	National security
☐	☐	Crops and/or livestock
☐	☐	Ecosystems
☐	☐	Any other significant area

Experiments of concern

Does the work involve any of these experiments of concern:

No	Yes	
☐	☐	Demonstrate how to render a vaccine ineffective
☐	☐	Confer resistance to therapeutically useful antibiotics or antiviral agents
☐	☐	Enhance the virulence of a pathogen or render a nonpathogen virulent
☐	☐	Increase transmissibility of a pathogen
☐	☐	Alter the host range of a pathogen
☐	☐	Enable evasion of diagnostic/detection modalities
☐	☐	Enable the weaponization of a biological agent or toxin
☐	☐	Any other potentially harmful combination of experiments and agents